Error analysis for tropospheric NO_2 retrieval from space

K. F. Boersma, H. J. Eskes, and E. J. Brinksma
Royal Netherlands Meteorological Institute, De Bilt, Netherlands

Received 8 July 2003; revised 16 October 2003; accepted 1 December 2003; published 26 February 2004.

[1] Retrieval uncertainty estimates for vertical tropospheric NO_2 columns based on theoretical error source discussions combined with actual Global Ozone Monitoring Experiment (GOME) observations are presented. Contributions to the total retrieval uncertainty are divided into three categories: (1) errors caused by measurement noise and spectral fitting, affecting the slant column density, (2) errors related to the separation of stratospheric and tropospheric NO_2 affecting the estimate of the stratospheric slant column, and (3) errors due to uncertainty in model parameters such as clouds, surface albedo, and a priori profile shape, affecting the tropospheric air mass factor. Furthermore, it is shown that a correction for the effective temperature of the trace gas is essential and that a correction for the presence of aerosols needs to be accompanied by aerosol corrections to the cloud retrieval. A discussion of the error components and total retrieval uncertainty is given for March 1997. Tropospheric NO_2 columns can be retrieved with a precision of 35–60% over regions with a large contribution of the troposphere to the total column. This error estimate demonstrates the need for highly accurate albedo maps, cloud retrieval schemes, and realistic a priori NO_2 profile shapes. *INDEX TERMS:* 0360 Atmospheric Composition and Structure: Transmission and scattering of radiation; 0365 Atmospheric Composition and Structure: Troposphere—composition and chemistry; 0394 Atmospheric Composition and Structure: Instruments and techniques; 3360 Meteorology and Atmospheric Dynamics: Remote sensing; *KEYWORDS:* NO_2, retrieval, errors

Citation: Boersma, K. F., H. J. Eskes, and E. J. Brinksma (2004), Error analysis for tropospheric NO_2 retrieval from space, *J. Geophys. Res.*, *109*, D04311, doi:10.1029/2003JD003962.

1. Introduction

[2] It has been demonstrated with GOME on ESA ERS-2 [*Burrows et al.*, 1999] that satellites can observe trace gases in the troposphere, including contributions from the boundary layer. GOME and SCIAMACHY currently observe, and OMI is soon expected to observe, several key species of tropospheric chemistry, such as O_3 [e.g., *Valks et al.*, 2003], NO_2 [e.g., *Leue et al.*, 2001], HCHO [e.g., *Chance et al.*, 2000], BrO [e.g., *Wagner and Platt*, 1998] and SO_2 [e.g., *Eisinger and Burrows*, 1998]. Column amounts of these trace gases have been retrieved using the Differential Optical Absorption Spectroscopy (DOAS) technique [e.g., *Platt*, 1994]. They contain important information on fossil fuel burning emissions, biogenic hydrocarbon emission, biomass burning, NO_x produced by lightning, and volcano emissions.

[3] There are three reasons to quantify the errors in current and future tropospheric retrievals.

[4] 1. In the past two years, several papers [*Leue et al.*, 2001; *Velders et al.*, 2001; *Martin et al.*, 2002, 2003; *Richter and Burrows*, 2002; *Lauer et al.*, 2002] have been published on the retrieval of tropospheric NO_2 from GOME. Although these papers paid substantial attention to retrieval errors in a general sense, none of them discussed the uncertainties of the retrieved tropospheric columns on a quantitative, pixel-to-pixel basis. Since the ultimate goal is to make satellite data available to users for quantitative regional air pollution monitoring, pollution trend studies and budget calculations, realistic quantitative estimates of the columns and their errors are essential and should be given for every individual retrieval.

[5] 2. Tropospheric retrieval methods are relatively young and unvalidated. One step in convincing potential users that the retrieved columns are quantitative and accurate, is to provide a realistic uncertainty estimate along with the columns.

[6] 3. Retrieval methods have to contend with a multitude of uncertainties that are related to the satellite instrument and to a priori model parameters. Information on how individual model parameters influence the retrieval is crucial to assess the errors in the retrieval method, and provides guidelines to improve future retrievals.

[7] A short introduction on the retrieval method is given in section 2. This section also describes how individual uncertainties propagate into the final uncertainty estimate of the tropospheric column density, followed by a discussion of the numerical approach in section 3. Sections 4–6 treat the individual error sources, section 7 summarizes our findings, and, finally, section 8 presents conclusions and discusses directions for future research.

2. Retrieval Method

2.1. DOAS Approach

[8] The main retrieval approach for GOME, SCIAMACHY and OMI nadir products is the DOAS method. This method consists of two steps:

0148-0227/04/2003JD003962$09.00

[9] 1. A spectral fit within a predefined window of a set of relevant reference spectra to a satellite-measured reflectance (defined as the top-of-atmosphere ratio of radiance times π to solar irradiance on a horizontal surface unit) spectrum. Characteristic is the division of the reflectance spectrum into a spectrally smooth part, modeled by a polynomial, and in a differential part from which trace gas information is retrieved. This step determines the slant column density of a trace gas, which is interpreted as the column density along the average photon path from the Sun through the atmosphere to the satellite instrument.

[10] 2. The application of an air mass factor to convert the slant column into a vertical column. For practical applications of DOAS it is important that the trace gas under investigation has a small absorption optical thickness in the predefined spectral window. For example, NO_2 has a typical slant optical thickness of 0.005 (at 440 nm with a typical vertical column of 3.0×10^{15} molec. cm^{-2} and an air mass factor of 2.8).

[11] Let **R** be our DOAS retrieval method to compute a vertical column density $\hat{x}$ based on the measured reflectance spectrum **y**, the a priori trace gas profile information $\mathbf{x}_a$ and the best estimate of the forward model parameters $\hat{\mathbf{b}}$ (our notation follows *Rodgers* [2000]). The set of model parameters $\hat{\mathbf{b}}$ includes cloud fraction, cloud height, surface albedo, and aerosol optical thickness vertical distribution. We can then write our retrieval **R** in terms of the two DOAS steps,

$$\hat{x} = \mathbf{R}\left(\mathbf{y}, \hat{\mathbf{b}}, \mathbf{x}_a\right) = \frac{N_s(\mathbf{y})}{M\left(\mathbf{x_a}, \hat{\mathbf{b}}\right)} \tag{1}$$

The air mass factor M depends on the a priori trace gas profile $\mathbf{x}_a$ and the (best estimate) forward model parameters $\hat{\mathbf{b}}$. Strictly speaking, the slant column density $N_s(\mathbf{y})$ also depends on $\mathbf{x}_a$ through the temperature-dependent absorption cross-section but we assume here and show later that this can be efficiently corrected for a posteriori.

[12] For small optical thickness, M can be written as follows [*Palmer et al.*, 2001]:

$$M = \frac{\sum_l m_l\left(\hat{\mathbf{b}}\right) x_{a,l}}{\sum_l x_{a,l}} \tag{2}$$

with $m_l = \partial N_s / \partial x_l$ the elements of the altitude-dependent air mass factor as computed from a radiative transfer model. The altitude-dependent air mass factor is computed in the same way as the total air mass factor, but for an optically thin amount of trace gas x_l in layer l only. For small optical absorption thickness, the trace gas has a negligible effect on the radiation field, the slant column is a linear sum of contributions from individual layers, and m_l is independent of $\mathbf{x}_a$. The vector elements of $\mathbf{x}_a$ are represented by $x_{a,l}$, the a priori subcolumn (in molec. cm^{-2}) for layer l.

2.2. DOAS for Tropospheric Trace Gases

[13] When a trace gas resides in the stratosphere only, the computation of the air mass factor can be well approximated by a simple geometrical form, valid for angles up to 70°,

$$M_{geo} = \frac{1}{\cos(\theta_0)} + \frac{1}{\cos(\theta)} \tag{3}$$

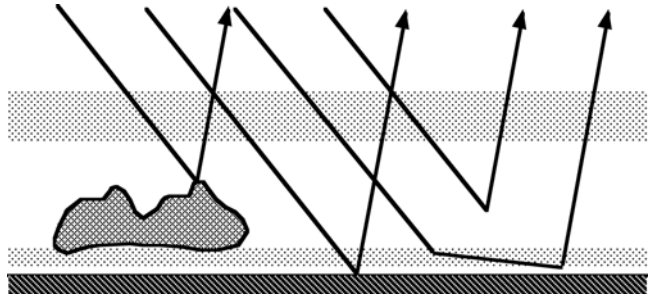

Figure 1. Several light paths (Sun to satellite) that contribute to the radiation as observed by GOME. The shaded areas indicate a trace gas residing in the stratosphere or in the lower troposphere.

Figure 1 illustrates how the light paths all cross the shaded area in the stratosphere in the same way. The length of the path in the stratosphere is determined completely by the solar zenith angle θ_0 and the viewing angle θ as specified by equation (3). This is a good approximation since only a small fraction of the light is scattered within the stratosphere. Stratospheric nadir UV/VIS retrievals are thus relatively insensitive to a priori assumptions on the state of the atmosphere. For example, reported uncertainties on GOME vertical ozone columns are generally below 5% [e.g., *Balis et al.*, 2001].

[14] For trace gases in the boundary layer (BL) and free troposphere, the air mass factor computation is much more sensitive to parameters $\hat{\mathbf{b}}$. As indicated in Figure 1, light is reflected from the surface, and scattered by cloud particles, air molecules and aerosols, and the photon path distribution in the troposphere is complicated. Satellite UV-VIS spectrometers exhibit a strongly modified sensitivity to the lowest atmospheric layers, to be obtained from a full radiative transfer computation combined with knowledge of the trace gas profile shape (equation (2)). Such calculations depend directly on the surface albedo, cloud properties, aerosols and a priori profile shape. *Leue et al.* [2001] have reported air mass factors 2.5 times lower than air mass factors calculated with equation (3) and much larger correction factors are expected for BL NO_2 in combination with small surface albedo.

[15] In the optically thin limit, relevant for NO_2, the total slant column density is conveniently written as the sum of the stratospheric and tropospheric (slant) columns ($\hat{x} = \hat{x}_{tr} + \hat{x}_{st}$). The tropospheric vertical column becomes

$$\hat{x}_{tr} = \frac{N_s(\mathbf{y}) - N_{s,st}}{M_{tr}\left(x_{a,tr}, \hat{\mathbf{b}}\right)} \tag{4}$$

where $N_{s,st}$ is the stratospheric component of the slant column, and M_{tr} represents the tropospheric air mass factor. The tropospheric air mass factor is obtained by inserting a troposphere-only a priori NO_2 profile in equation (2).

2.3. DOAS Error Analysis

[16] The three terms in equation (4) are error sources in the computation of the tropospheric column density. These terms are assumed to be mutually uncorrelated, since they arise from nearly independent retrieval steps. Neglecting

forward model errors, the error variance of the tropospheric column is

$$\begin{aligned}\sigma^2_{\hat{x}_{tr}} &= \langle \epsilon^2_{\hat{x}_{tr}} \rangle \\ &= \left(\frac{\partial \hat{x}_{tr}}{\partial N_s}\right)^2 \sigma^2_{N_s} + \left(\frac{\partial \hat{x}_{tr}}{\partial N_{s,st}}\right)^2 \sigma^2_{N_{s,st}} + \left(\frac{\partial \hat{x}_{tr}}{\partial M_{tr}}\right)^2 \sigma^2_{M_{tr}} \\ &= \left(\frac{\sigma_{N_s}}{M_{tr}}\right)^2 + \left(\frac{\sigma_{N_{s,st}}}{M_{tr}}\right)^2 + \left(\frac{(N_s - N_{s,st})\sigma_{M_{tr}}}{M^2_{tr}}\right)^2 \end{aligned} \quad (5)$$

where $\langle \epsilon^2_{\hat{x}_{tr}} \rangle$ represents the expectation value of the squared deviation from the true column. σ_{N_s} is the slant column density precision, $\sigma_{N_{s,st}}$ the standard deviation of stratospheric slant column density errors, and $\sigma_{M_{tr}}$ denotes the standard deviation of the errors in the tropospheric air mass factor. The total error depends on details in the retrieval, and therefore differs from one pixel to the next. For small tropospheric excess slant columns ($N_s - N_{s,st}$), the overall retrieval uncertainty is dominated by the errors in N_s and $N_{s,st}$, whereas for large tropospheric slant columns, the retrieval uncertainty is dominated by air mass factor uncertainties (the last term in equation (5)).

[17] It is important to clarify the meaning of the retrieval errors presented in this work. The largest uncertainties in the retrieval of tropospheric trace gases are due to errors in the description of clouds, albedo, profile shape and aerosols. It is important to realize that all these errors are systematic in nature, and all have their own temporal and spatial scale. In principle, one would like to distinguish "random" errors from persistent errors in the radiation modeling. In practice this is very complicated. This is similar to the treatment of model errors in data assimilation. Despite the fact that such model errors are also systematic in nature with correlations in both space and time, they are normally treated as random errors. Only the most obvious bias (time-independent model drift) is sometimes treated separately. The retrieval parameters N_s, $N_{s,st}$ and $\hat{\mathbf{b}}$ discussed below will therefore contain error components with various time and space correlation scales. A few examples: (1) The albedo maps used have a finite resolution, and as a result the albedo near boundaries between high (desert) and low (sea) albedo will be in error. This error has only a small correlation length in space, but is of course correlated in time (time independent). Such errors will largely cancel when averaged over space. (2) The FRESCO cloud retrieval [*Koelemeijer et al.*, 2001] only provides cloud fraction and height, and is not able to distinguish thick, localized clouds from thin extended clouds. Such errors will not be very correlated in time (clouds change rapidly on average), but there will be (limited) correlations in space related to these errors. (3) There are systematic errors in $\mathbf{x}_a$ resulting from the model. For example vertical transport may be modeled correctly in the model for stable meteorological regimes, but may lead to errors in profile shape in times of strong meteorological activity. The model resolution will play an important role as well. Such model related errors range from time-independent (possible systematic problems in the modeling of vertical transport) to errors with short timescales (subgrid-scale convective activity). Systematic error components of forward model parameters may not average to zero over time for certain regions or specific periods.

[18] The DOAS retrievals can be used in two ways, each with its own error estimate:

[19] 1. The total column estimate can be studied and/or compared with independent measurements of the column amount. The error estimate belonging to the tropospheric subcolumn is discussed above (equation (5)).

[20] 2. For comparisons with chemistry-transport models, validation with independent profile measurements and for data assimilation purposes, averaging kernel information (when available) should be used [*Eskes and Boersma*, 2003]. The error estimate is smaller than the one discussed above: The a priori profile shape error (or the "smoothing error" [*Rodgers*, 2000]) no longer contributes, as demonstrated below.

[21] Averaging kernels $\mathbf{A}$ provide the relation between the retrieved column and the true profile: $\hat{x} - x_a = \mathbf{A}(\mathbf{x} - \mathbf{x}_a)$, or, for weak absorbers, $\hat{x} = \mathbf{A}\mathbf{x}$. The relative difference δ between the retrieval $\hat{x}$ and an independent profile $\mathbf{x}_i$ is

$$\delta = \frac{\hat{x} - \mathbf{A}\mathbf{x}_i}{\hat{x}} \quad (6)$$

The expression for the DOAS kernel in terms of the height-dependent air mass factor [*Eskes and Boersma*, 2003] is

$$\mathbf{A}\mathbf{x}_i = \frac{\sum_l m_l(\hat{\mathbf{b}}) x_{i,l}}{M(\mathbf{x}_a, \hat{\mathbf{b}})} \quad (7)$$

and $\hat{x} = N_s/M(\mathbf{x}_a, \hat{\mathbf{b}})$. The total air mass factor M appears as the denominator of both $\hat{x}$ and $\mathbf{A}$, and can therefore be divided out in equation (6). Because only M depends on $\mathbf{x}_a$, the comparison through the averaging kernel is not influenced by a badly chosen a priori profile shape. The DOAS retrieval error for the comparison in equation (6) now consists of error contributions from the slant column N_s and from representativeness errors in the height-dependent air mass factor m_l. The latter has contributions from errors in the model parameters $\hat{\mathbf{b}}$, i.e., surface albedo, cloud parameters and aerosols. These model parameter and slant column related errors are identical to the corresponding error contributions to the total column (case 1) and are discussed in the sections below. Although this discussion focused on the total column, the arguments hold just as well for the tropospheric column (replace M by M_{tr} and so on).

3. Numerical Approach

3.1. Retrieval Approach

[22] The starting point of our retrieval is a set of slant column densities obtained from the Institut für Umweltphysik of the University of Heidelberg (hereafter IUP) [*Wagner et al.*, 1999]. The IUP slant columns are retrieved using a fixed solar reference spectrum (measured on 1 June 1997 and discussed further in section 4) and an assumed atmospheric NO_2 temperature of 221 K.

[23] The stratospheric slant column is determined with two approaches, namely (1) the reference sector method [*Richter and Burrows*, 2002; *Martin et al.*, 2002] and (2) data assimilation of observed slant column densities in a chemistry-transport model proposed by H. J. Eskes and K. F. Boersma (manuscript in preparation, 2004) and described by *Eskes et al.* [2003]. Shortly summarized, GOME slant column observations are assimilated in TM3 as follows:

[24] 1. A priori NO_2 profiles are convolved with the averaging kernel to give the model predicted slant column densities ($N_{s,m} = M\mathbf{Ax_a}$).

[25] 2. The differences between the observed and modeled columns are used to force the modeled columns to generate an analyzed state based on the model forecast and GOME observations. This forcing depends on weights (from observation representativeness and model errors) attributed to both modeled and observed columns. Observed columns are attributed a low weight if the model predicts large tropospheric columns, thus minimizing the influence of slant columns contaminated by tropospheric signals. The forcing equation is solved with the statistical interpolation method, involving a covariance matrix operator that incorporates the assumed 3-D correlation of NO_2 differences. The most important characteristics of this forecast covariance matrix are as follows: (1) the conservation of model profile shapes; that is, differences between modeled and observed quantities are not vertically redistributed but rather scaled in the forcing equation, and (2) the horizontal correlation model function is assumed to follow a Gaussian shape with a 1/e correlation length of 600 km.

[26] 3. The forecast field is subsequently replaced by the analysis. This cycle is repeated for all available orbits, and gives zero mean differences between observed and analyzed fields after approximately 80 orbits (6 days) of GOME data.

[27] The advantage of the approach is that slant column variations due to stratospheric dynamics are now accounted for. The aim is to decrease the threshold of tropospheric columns that can be retrieved. An additional advantage is that the assimilation scheme provides a statistical estimate of the uncertainty in the stratospheric slant column.

[28] The air mass factor calculation is coupled to cloud cover and cloud height retrievals from the O_2-A band based FRESCO algorithm. Surface albedo input is obtained on the basis of the TOMS and GOME Lambert Equivalent Reflectivity (LER) data sets, as outlined in section 6.3. The advantage of taking ancillary data derived from the same satellite instrument is the consistency concerning the pixel footprint, the treatment of clouds, and viewing geometry. A priori NO_2 profile shapes are obtained from the TM3 chemistry-transport model, as described in section 3.3. A global 3-D chemical-transport model is currently considered the best source for profile shapes of NO_2 given the lack of measured tropospheric NO_2 profiles and the variability in profile shapes. TM3 a priori NO_2 profiles are produced for the GOME ground pixel position and time. A temperature correction of the slant column densities, necessary because of the assumed fixed atmospheric NO_2 temperature of 221 K, is performed on the basis of ECMWF temperature fields combined with the a priori NO_2 profile shapes, as described in section 4.

3.2. Computation of the Altitude-Dependent Air Mass Factor

[29] The altitude-dependent air mass factors are computed with the Doubling Adding KNMI (DAK) radiative transfer code. DAK is based on the polarized doubling-adding method [*de Haan et al.*, 1987] that accurately accounts for multiple scattering. The polarized internal radiation field of the atmosphere is described by *Stammes et al.* [1989]. The model atmosphere consists of a Lambertian surface albedo, and an arbitrary number of atmospheric layers, each of which can have Rayleigh scattering, gas absorption, and aerosol particle absorption and scattering. In this version of DAK, Raman scattering is not taken into account, and the plane-parallel approximation is used, therefore viewing geometries are restricted to less than 70°.

[30] The constructed air mass factor look-up table is based on DAK, and is a function of 6 parameters: solar zenith angle θ_0, viewing zenith angle θ, relative azimuth angle ϕ, Lambertian surface albedo a_{sf}, surface pressure p_{sf}, and (midlevel) pressure p. The reason why aerosols are not included in the look-up table is explained in section 6.5.

3.3. Computation of the NO_2 Profiles

[31] Vertical distributions of NO_2 are calculated with the Tracer Model version 3 (TM3) [*Dentener et al.*, 2002, and references therein], a global transport chemistry model based on 6-hourly mean ECMWF meteorological fields and emission distributions taken from the emission database developed by *van Aardenne et al.* [2001]. This is based on estimates for the year 1990, emissions for 1997 are obtained by extrapolation of the 1990 emissions based on statistics from *Marland et al.* [2000]. This extrapolation is similar to OxComp model intercomparisons for the year 2000, organized in the preparation of the Intergovernmental Panel on Climate Change (IPCC) Third Assessment Report [*Prather et al.*, 2001]. The NO_x production from lightning discharges is coupled to convective precipitation in the model [*Meijer et al.*, 2001]. In this study, TM3 is applied with a spatial resolution of 5° longitude and 3.75° latitude. The vertical spacing, 19 levels up to 10 mbar, is defined according to the terrain following sigma coordinates near the surface, pressure coordinates in the stratosphere, and a hybrid of the two in between (ECMWF level definition). Tracer advection is simulated with the "slopes" scheme [*Russel and Lerner*, 1981]. Convective tracer transports are calculated with a mass flux scheme that accounts for shallow, midlevel and deep convection. Turbulent vertical transport is computed by a stability-dependent vertical diffusion scheme following *Louis* [1979].

[32] Photolysis rates are calculated with a parameterized radiative transfer scheme at seven characteristic wavelengths. The ozone mixing ratios at each model level are used as an input for the overhead ozone column. Cloud base height, cloud top height, and cloud optical thickness stem from the ECMWF operational data archive. Surface albedos depend on the surface characterization and include time-varying snow and ice. The surface characterization is also applied in the dry deposition scheme for gases and aerosols. Wet deposition is parameterized according to the scheme by *Guelle et al.* [1998] and accounts for both in-cloud and subcloud removal of gases and aerosols. The current chemical scheme includes tropospheric CH_4-CO-NMHC-NO_x-SO_x chemistry and accounts for 38 species, of which 15 are transported, 24 photolysis reactions, and 67 thermal reactions. Heterogeneous processes are handled according to *Dentener and Crutzen* [1994].

4. Uncertainty of the Slant Column Density

[33] The first error source in equation (4) is the slant column density. Instrument noise is a source of random

Table 1. Systematic Slant Column Errors

	Regular	Enhanced NO_2
NO_2 cross section	2%	2%
Spectral calibration	0.5%	0.3%
Temperature (potentially)	2%	−20%
Solar diffuser (GDP2.7)	3.0×10^{15} molec. cm^{-2}	3.0×10^{15} molec. cm^{-2}
Total	3%	−20–2%

error. Other aspects, such as imperfect wavelength calibration, laboratory reference spectra errors, and instrumental spectral features are considered to be systematic errors, since they are approximately constant in time.

[34] Difficulties with GOME operational spectral fitting have led to the suspicion that the GOME reflectance spectrum suffers from interfering variable diffuser plate spectral features that appear in the daily solar reference spectra. Apparent slant column densities as a result of spectral diffuser plate effects can be as large as 3.0×10^{15} molec. cm^{-2} (estimated from *Wenig* [2002]). One approach to avoid the day-to-day jumps in the reflectance spectra is to use a fixed solar reference spectrum (A. Richter and T. Wagner, personal communication, 2001). This approach, implemented in the IUP slant column retrieval, introduces a more or less fixed bias in the stratospheric slant columns, but has little to no impact on the retrieval of tropospheric columns. Careful comparison with independent measurements will have to provide an absolute reference to determine this bias (needed for total column retrievals) introduced by the fixed solar reference.

[35] Results of a sensitivity study to quantify slant column errors for the OMI NO_2 DOAS algorithm [*Boersma et al.*, 2002] are summarized in Table 1. Systematic slant column errors due to NO_2 cross section spectra are estimated from comparisons between various laboratory measurements of NO_2 cross section spectra which showed mutual agreement of 2% as discussed by *Vandaele et al.* [1998]. Errors due to spectral calibration uncertainties are taken from sensitivity studies performed for OMI; typical expected offsets of 0.002 nm resulted in errors smaller than 0.5%. Temperature errors are assumed to be random for most stratospheric retrievals given the estimated ECMWF temperature profile precision of a few degrees Kelvin. Note however, that our retrieval method does account for the temperature effect on the NO_2 cross section. Neglect of the temperature profile, and assuming a fixed atmospheric NO_2 temperature of 221 K, will result in large systematic errors of −20%, as discussed at the end of this section. OMI has somewhat different instrumental features than GOME (signal-to-noise ratio, spectral resolution) but the numbers approximately apply to GOME as well.

[36] An indication of the uncertainties in the slant columns can be obtained by comparing IUP slant columns with the official GOME Data Processor product (GDP2.7) slant columns [*Spurr and Thomas*, 2000] for March 1997. Despite the fact that both retrievals use the DOAS technique, there are also distinct differences, namely, (1) different fit windows; IUP uses a 425–450 nm, and GDP2.7 uses a 431–452 nm fit window, (2) different irradiance spectra; IUP uses a fixed solar reference spectrum, and GDP2.7 uses a daily solar reference spectrum, (3) differences in spectral fitting; for example differences in the use of ring spectra, undersampling correction, and assumed instrument transfer function. Comparing two independent data sets allows investigation of RMS differences as a measure for the combined uncertainty of the two data sets.

[37] The differences in spectral fitting procedures for IUP and GDP2.7 are tabulated in Table 2 from *Spurr and Thomas* [2000] for GDP2.7 and from *Wagner et al.* [1999] for IUP. In the comparison the GDP2.7 for the daily solar spectrum is corrected by subtracting the daily mean (spatially uniform) offset between the IUP and GDP2.7 data. Subsequently the Pearson correlation coefficient r between the IUP and corrected GDP2.7 slant columns is computed for March 1997, which is better than 0.99, indicating good agreement between the two data sets.

[38] To quantify the comparison between IUP and GDP2.7, the histogram of the slant column differences is plotted in Figure 2. The 1σ-level extracted from a Gaussian function equals 0.55×10^{15} molec. cm^{-2}. Assuming that both data sets are independent and contribute equally, the error on the slant column is estimated to be $0.4 \times 1\ 0^{15}$ molec. cm^{-2}. This number is consistent with slant column error estimates (4.3%, from *Wenig* [2002]) from measurement noise alone.

[39] It is common practice to use an absorption cross-section with a fixed temperature for the slant column density fit. Within the IUP and GDP2.7 fitting windows, the shape of the cross-section spectrum hardly changes, but the amplitude does change with temperature [*Burrows et al.*, 1998]. By fitting GOME reflectance spectra with NO_2 cross-sections measured at different temperatures, we found that the temperature dependence of the DOAS slant column fit is well described on the 425–450 nm interval by the correction term c_l for layer l expressed as

$$c_l = \frac{221 - 11.4}{T_l - 11.4} \tag{8}$$

with T_l the temperature in layer l and for a 221 K cross-section temperature used in the fit. Tests carried out with cross-section spectra by *Vandaele et al.* [1998] convolved with the OMI slit function yield similar results as described by *Boersma et al.* [2002]. The correction term c_l thus represents the ratio of the NO_2 slant column derived with a NO_2 cross section at T_l to the column derived at 221 K., i.e., $c_l = 1$ for NO_2 in a layer with mean temperature 221 K.

[40] The air mass factor calculation (equation (2)) is modified as

$$M = \frac{\sum_l m_l(\hat{\mathbf{b}}) x_{a,l} c_l}{\sum_l x_{a,l}} \tag{9}$$

In our approach, temperature correction terms based on equation (8) are used together with ECMWF temperature

Table 2. Slant Column Density Retrieval Characteristics

	GDP2.7	IUP
Fitting window	425–450 nm	431–452 nm
Fit parameters	O_3, ring, O_2-O_2, H_2O	O_3, ring, O_2-O_2, H_2O
Fitting method	nonlinear least squares	nonlinear least squares
Temperature	221 K	221 K
Solar reference	daily	fixed
Uncertainty in N_s	N/A	4.3%

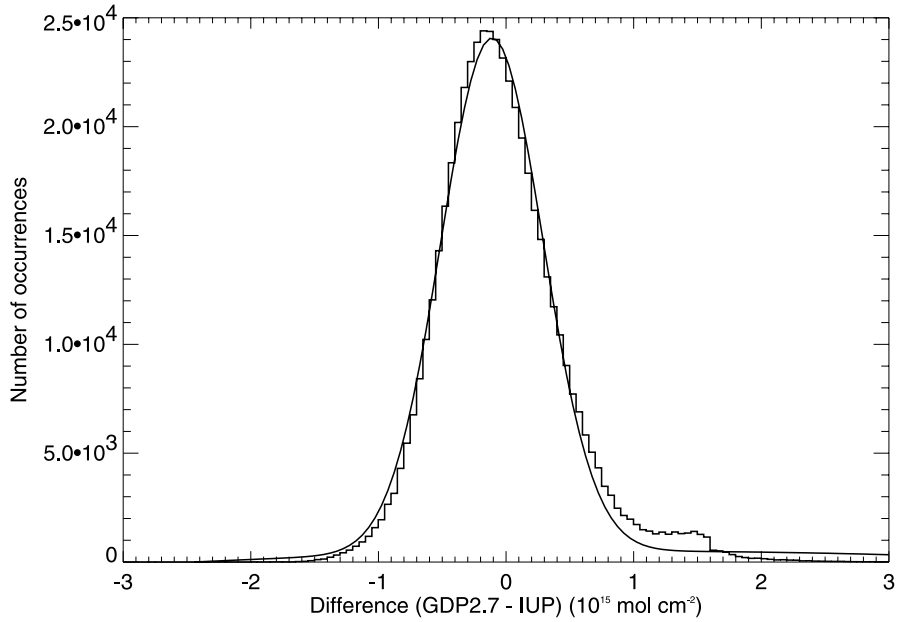

Figure 2. Histogram of the differences between GDP2.7 and IUP slant columns.

profiles and TM3 NO_2 profiles in equation (9). Figure 3 illustrates the monthly averaged errors that are expected in the slant column density if the temperature dependence of the NO_2 cross section would not be corrected for. In situations of tropospheric pollution (eastern United States, Northwest Europe, eastern Asia), the slant column would be underestimated by up to 20%. The stratospheric slant column would be systematically overestimated by up to 10% if the cold vortex is sampled by GOME. ECMWF 6 hour forecast temperature profiles used in TM3 are estimated to be accurate up to a few degrees Kelvin [see, e.g., *Knudsen*, 2003]. Temperature errors of a few degrees Kelvin lead to errors in the temperature correction of approximately a percent, which is neglected given the magnitude of other error sources discussed in this paper.

5. Uncertainty of the Stratospheric Slant Column

[41] The second error source in equation (4) is the estimate of the stratospheric slant column. The stratosphere-troposphere separation techniques introduced in the literature are based on the observation that stratospheric NO_2 has a smooth spatial behavior, and that tropospheric contributions occur locally over land near source regions, and are negligible over the oceans away from coastal regions. Table 3 summarizes the methods reported in the literature with their estimated uncertainties. Four methods can be distinguished:

[42] 1. The first method is the image processing technique (hereafter IPT) [*Leue et al.*, 2001]. In this method, land masses and cloud-free pixels are masked out, and on the basis of the remaining pixels, the stratospheric column is estimated using an image-processing filter that interpolates for the gaps. The implicit assumption is that over oceanic, cloudy pixels, the retrieved column is in fact the stratospheric column. This is a potential weakness of the method since tropospheric NO_2 may still be present above a cloud.

[43] 2. The second method is the reference sector method [*Richter and Burrows*, 2002; *Martin et al.*, 2002]. The stratospheric column is approximated by taking the average total columns over a remote Pacific region, and is assumed to be independent of longitude. The main advantage of this method is that the assumption of zero tropospheric NO_2 over cloud-covered pixels is not made; however, the drawback is that one needs to assume longitudinally homogeneous NO_2, whereas the IPT technique at least partially accounts for longitudinally varying NO_2. Furthermore, a small amount of tropospheric NO_2 may still be present in the reference sector pixels themselves, although *Martin et al.* [2002] correct for this by subtraction of the tropospheric amount taken from a CTM.

[44] 3. The third method is CTM stratosphere [*Richter et al.*, 2002]. In this method the stratospheric contribution is obtained from a chemical transport model. The main advantage is that the model accounts for dynamical features in stratospheric NO_2, but the drawback is that the retrieval of tropospheric NO_2 now depends quantitatively on a CTM.

[45] 4. The fourth method is data assimilation [*Eskes et al.*, 2003]. A CTM stratosphere is made consistent with the observations by assimilating the GOME NO_2 data as described in section 3.1. The advantage of this method over the CTM stratosphere, is that the dynamical features in stratospheric NO_2 are still predicted by the model, but that the model stratosphere is now driven by the actual GOME observations.

[46] The error associated with the assumption of zonally invariant stratospheric NO_2 is quantified by analyzing GOME stratospheric NO_2 data. Therefore a method is used that takes the mean over 2.5° cells within the 180–160° W longitudinal band to represent the daily global stratospheric vertical column. Generally, between 5 and 30 pixels are found within a reference sector cell, corresponding to a stratospheric vertical column precision $<0.25 \times 10^{15}$ molec. cm^{-2}. The spatiotemporal variability of stratospheric

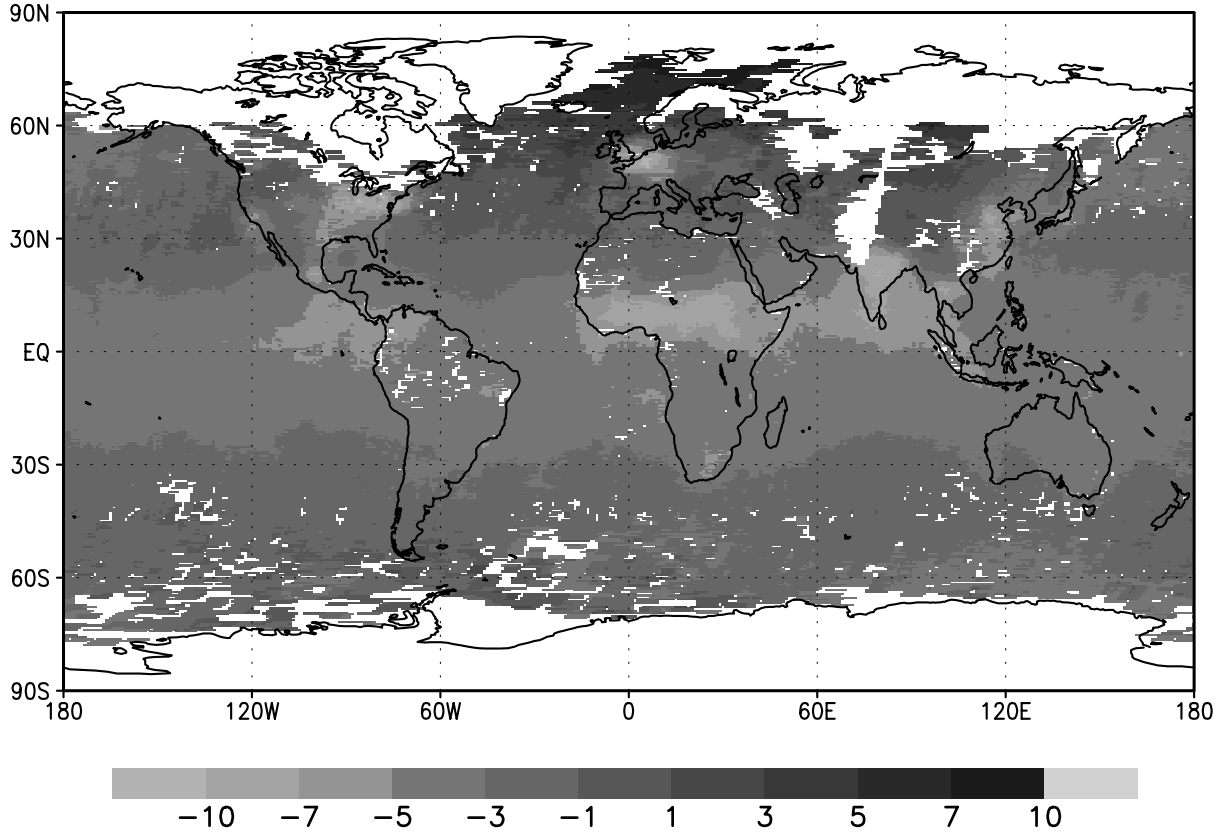

Figure 3. Systematic effect (%) of not accounting for atmospheric temperature variations in slant column retrieval for March 1997. Only pixels with a cloud radiance fraction smaller than 0.5 were taken. See color version of this figure at back of this issue.

NO_2 along a zonal band is a consequence of stratospheric dynamical processes that occur on various temporal and spatial scales. Synoptic-scale variability causes day-to-day changes in the total column. On top of this there are persistent (planetary wave related) variations that will influence the monthly or seasonal averages.

[47] Stratospheric NO_2 columns are defined as those observations that have model predicted vertical tropospheric NO_2 columns $<0.2 \times 10^{15}$ molec. cm^{-2}. The standard deviation of the 2.5° latitude bands is considered to be the sum of the zonal variability and the measurement noise. As an approximation to the measurement noise, the variability of the GOME observations within a 20° longitude box was computed and plotted for March 1997 in Figure 4. Note that the box variability (dash-dotted line) and the variability in the Reference Sector are in good agreement. The total standard deviation shows a minimum at the equator of approximately 0.25×10^{15} molec. cm^{-2}, and are smaller than 0.45×10^{15} molec. cm^{-2} at all latitudes. By correcting the total standard deviation for variability within the longitude boxes, the dynamical variability within a zonal band was quantified (solid line). Figure 4 shows that within the 20°S to 20°N region, box variability and zonal variability contribute approximately equally to the total standard deviation. At higher latitudes, however, dynamical variability dominates. The relative maximum around 30°S is attributed to variability due to the South Atlantic Anomaly.

[48] Another method, in which slant column observations were assimilated in a chemistry-transport model, resulted in a vertical column uncertainty estimate (standard deviation of the differences between model forecast and observed stratospheric NO_2) of approximately 0.2×10^{15} molec. cm^{-2}. This shows that data assimilation has the potential to reduce the uncertainties due to stratospheric dynamics. The error

Table 3. Uncertainties in the Estimation of the Stratospheric Vertical Column Density

Authors	Method	Temporal Coverage	Longitudes	Uncertainty
Leue et al. [2001]	IPT	3 days	0–360	3–20%
Velders et al. [2001]	IPT	3 days	0–360	10%
Richter and Burrows [2002]	ref. sector	3 days	180–190	15%
Martin et al. [2002][a]	ref. sector	daily	130–280	$<0.2 \times 10^{15}$ molec. cm^{-2}
Richter et al. [2002]	CTM reference	daily	0–360	not given
This work[b]	ref. sector	daily	180–200	$<0.45 \times 10^{15}$ molec. cm^{-2}
This work	assimilation	daily	0–360	$<0.2 \times 10^{15}$ molec. cm^{-2}

[a]Computed for the month of July.
[b]Computed for the month of March.

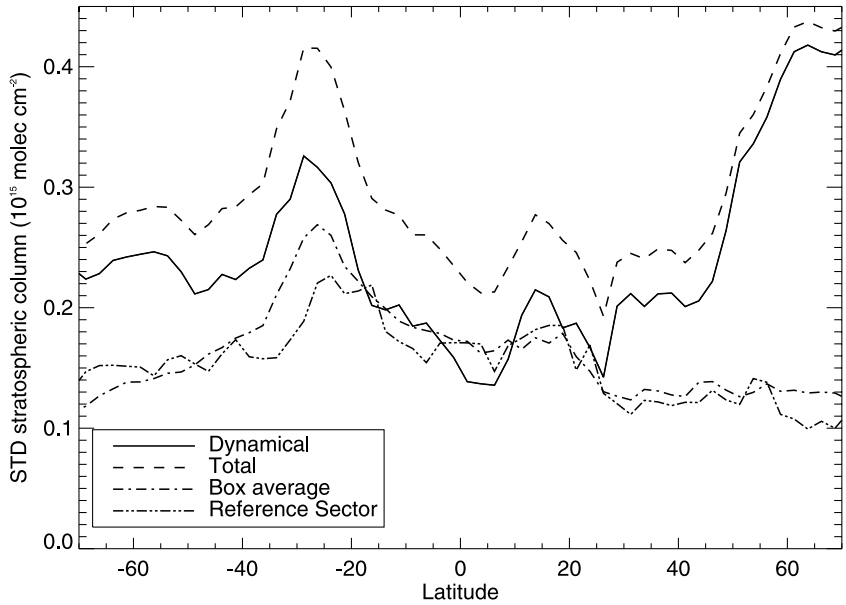

Figure 4. Zonal standard deviation of GOME stratospheric NO_2 columns for March 1997. The solid line is the estimated contribution of dynamical variability. The dashed line is the total standard deviation over a zonal band. The box average standard deviation is an estimate of the contribution of measurement noise to the total standard deviation. The reference sector standard deviation is a measure for the variability within the reference sector box (180°–160°W).

estimates resulting from the data assimilation approach will be used in the sections below.

6. Uncertainty of the Tropospheric Air Mass Factor

[49] The third and most critical error source in equation (4) is the tropospheric air mass factor. The air mass factor depends on the a priori assumed profile shape $\mathbf{x}_{a,tr}$ and four model parameters $\hat{\mathbf{b}}$,

$$M_{tr} = M\left(\mathbf{x}_{\mathbf{a,tr}}, \hat{\mathbf{b}}\right) = M\left(\mathbf{x}_{\mathbf{a,tr}}, f_{cl}, z_{cl}, a_{sf}, \boldsymbol{\tau}_{\mathbf{aer}}\right), \tag{10}$$

where f_{cl} is cloud fraction, z_{cl} is cloud (top) height, a_{sf} is surface albedo, and $\boldsymbol{\tau}_{\mathbf{aer}}$ denotes the aerosol optical thickness profile. The air mass factor depends on the solar zenith, viewing zenith and relative azimuth angle as well, but the measurement geometry is known with high accuracy and therefore does not contribute significantly to $\sigma_{M_{tr}}$. For the purpose of error analysis we linearize the air mass factor around the true values of the model parameters ($\mathbf{x}_{\mathbf{a,tr}}^{\mathbf{true}}$, f_{cl}^{true} z_{cl}^{true}, a_{sf}^{true}, $\boldsymbol{\tau}_{\mathbf{aer}}^{\mathbf{true}}$)

$$\begin{aligned} M_{tr} = {} & M\left(\mathbf{x}_{\mathbf{a,tr}}^{\mathbf{true}}, f_{cl}^{true}, z_{cl}^{true}, a_{sf}^{true}, \boldsymbol{\tau}_{\mathbf{aer}}^{\mathbf{true}}\right) \\ & + \frac{\partial M}{\partial \mathbf{x}_{\mathbf{a,tr}}}\left(\mathbf{x}_{\mathbf{a,tr}} - \mathbf{x}_{\mathbf{a,tr}}^{\mathbf{true}}\right) + \frac{\partial M}{\partial f_{cl}}\left(f_{cl} - f_{cl}^{true}\right) \\ & + \frac{\partial M}{\partial z_{cl}}\left(z_{cl} - z_{cl}^{true}\right) + \frac{\partial M}{\partial a_{sf}}\left(a_{sf} - a_{sf}^{true}\right) \\ & + \frac{\partial M}{\partial \boldsymbol{\tau}_{\mathbf{aer}}}\left(\boldsymbol{\tau}_{\mathbf{aer}} - \boldsymbol{\tau}_{\mathbf{aer}}^{\mathbf{true}}\right) \end{aligned} \tag{11}$$

We define $\mathbf{K} = \partial M/\partial \mathbf{b}$ as the sensitivity of the air mass factor to quantity $\mathbf{b}$. The air mass factor covariance is

$$\begin{aligned} \langle \epsilon_M^2 \rangle &= \left\langle \left(\sum_{b=1}^{5} K_b \epsilon_b \right)^2 \right\rangle \\ &= \left\langle \left(K_{\mathrm{x_{a,tr}}} \epsilon_{\mathrm{x_{a,tr}}} + K_{f_{cl}} \epsilon_{f_{cl}} + K_{z_{cl}} \epsilon_{z_{cl}} + K_{a_s} \epsilon_{a_s} + K_{\tau_{aer}} \epsilon_{\tau_{aer}} \right) \right\rangle^2 \\ &= \sum_{b,b'=1}^{5} K_b K_{b'} \langle \epsilon_b \epsilon_{b'} \rangle \end{aligned} \tag{12}$$

where $\sigma_b = \sqrt{\langle \epsilon_b^2 \rangle}$ (with $\epsilon_b = (b - b^{true})$) represents the error in our knowledge of the quantities b. It is important to realize that equation (12) allows the calculation of the pixel-specific air mass factor uncertainty, since every individual retrieval scene has a unique combination of model parameters and therefore a unique set of model parameter sensitivities. The uncertainty in the air mass factor is $\sigma_M = \sqrt{\langle \epsilon_M^2 \rangle}$.

[50] In computing the uncertainty in the air mass factor, we need to take into account the error covariance terms $\langle \epsilon_b \ \epsilon_b' \rangle$. The diagonal elements of the covariance are the subject of the sections below. The appendix discusses the off-diagonal elements.

6.1. Errors Due to Cloud Fraction

[51] The air mass factor for a partly clouded scene is determined with the independent pixel approximation, which assumes that the air mass factor can be written as a linear combination of a cloudy and a clear air mass factor,

$$M_{tr} = wM_{cl} + (1 - w)M_{cr} \tag{13}$$

where M_{cl} is the air mass factor for a completely cloud-covered scene, and M_{cr} is the air mass factor for a completely cloud-free pixel. The radiance-weighted cloud fraction w is defined as

$$w = \frac{f_{cl} I_{cl}}{f_{cl} I_{cl} + (1 - f_{cl}) I_{cr}} \quad (14)$$

with f_{cl} the cloud fraction as obtained from FRESCO. I_{cl} and I_{cr} are the fit window averaged radiances for 100% cloudy and clear scenes respectively. I_{cl} mainly depends on the viewing geometry and assumed cloud albedo [*Koelemeijer et al.*, 2001]. I_{cr} depends on surface albedo and viewing geometry. Values for I_{cl} and I_{cr} are obtained from *Vermote and Tanré* [1992]. The air mass factor for a completely clouded pixel is obtained with equation (9), with $m_l = 0$ below cloud height.

[52] For $\sigma_{f_{cl}}$ we use the reported uncertainty of the FRESCO cloud fraction (0.05, *Koelemeijer et al.* [2001]). Figure 5a shows the theoretical sensitivity of the air mass factor to f_{cl}, for the case of a heavily polluted profile over northwest Europe, and a remote unpolluted profile over the Pacific.

[53] The overall magnitude of cloud fraction-related errors is plotted in Figure 6a. More than 500.000 GOME pixels in March 1997 were taken and filtered for cloud radiance fractions <50% (cloud fractions approximately <15%) to ensure a strong signal from the BL. Over continental regions with high tropospheric NO_2 columns, typically uncertainties up to 30% occur.

[54] Three groups of measurements may be distinguished: unpolluted ($\hat{x}_{a,tr} < 0.3 \times 10^{15}$ molec. cm^{-2}, 30% of the pixels), moderately polluted ($0.3 < \hat{x}_{a,tr} < 1.0 \times 10^{15}$ molec. cm^{-2}, 41%) and heavily polluted ($\hat{x}_{a,tr} > 1.0 \times 10^{15}$ molec. cm^{-2}, 29%). The value of 0.3×10^{15} molec. cm^{-2} corresponds to a realistic threshold for detection by GOME. We did not include any pixels with negative values (occurring if $N_{s,st} > N_s$) in our analysis. Subsequently the mean of the uncertainties of all pixels for these groups is calculated, and the results are summarized in Table 4. This table gives an impression of the overall uncertainty in M_{tr} as a consequence of uncertainties in the cloud fraction. Table 4 shows that the uncertainty depends on the tropospheric NO_2 load and is largest for the polluted pixels near source regions. This table presents a summary of a vast quantity of realistic retrieval scenarios. Tropospheric air mass factors and their uncertainties have been computed for very different combinations of cloud height, surface albedo, and profile shape. On the basis of this analysis, it can be concluded that, on average, tropospheric air mass factor uncertainties due to cloud fraction uncertainties are in the 0–30% range, with 20–30% uncertainties for polluted regions with small cloud fractions.

6.2. Errors Due to Cloud Height

[55] Figure 5b illustrates the sensitivity of the air mass factor to the cloud height. This sensitivity is strongest when the cloud is located in altitude regimes in which NO_2 concentrations are largest. However, for most retrieval scenarios the FRESCO cloud tops are well above the pollution layers. Cloud top errors induce retrieval errors that are on average less than 10%. Cloud height does not seem to matter (uncertainty <2%) over the heavily polluted areas in the Northern Hemisphere.

[56] The air mass factor uncertainties due to cloud top uncertainties are higher in "outflow" areas because the clouds tops are lower and therefore nearer to the tropospheric NO_2 outflow plumes. Figure 6b summarizes the uncertainty in March 1997 retrievals that were done only for pixels with cloud tops situated between the surface and 800 hPa. It shows that low FRESCO clouds occur mostly over the (sub-)tropical oceans and sometimes over coastal regions. The figure illustrates that sea pixels in the vicinity of source regions exhibit uncertainties up to 25%, in line with the expectation of relatively high NO_2 concentrations close to the cloud height.

6.3. Errors Due to Surface Albedo

[57] In our retrieval, a Lambertian surface is assumed, so that the Lambert-equivalent reflectivity (LER) is taken to be the surface albedo. The LER has a large impact on the value of the tropospheric air mass factors through the radiative transfer calculations as described in section 3.2. The monthly averaged LER maps used in this study were constructed in the following way. The TOMS 380 nm LER data set [*Herman and Celarier*, 1997] is ratioed to the GOME 380 nm data set [*Koelemeijer et al.*, 2003] for the month of March. A 440 nm Lambertian equivalent surface reflectivity is constructed as follows:

$$a_{sf}(440) = \frac{a_{sf,GOME}(440)}{a_{sf,GOME}(380)} a_{sf,TOMS}(380) \quad (15)$$

By doing so, we combined the strengths of both data sets, namely the long-term TOMS record (1978–1992) and the spectral information (11 wavelengths) of the shorter GOME record (1995–2001).

[58] To estimate albedo uncertainties, the GOME 440 nm LER and constructed 440 nm LER were compared for latitudes between 60°N and 60°S. From Figure 7 it can be seen that the absolute difference between the GOME and TOMS data sets is below 0.006, which is less than the TOMS discrete step value of 0.01. The fitted exponential probability function corresponds to a 1σ value of 0.013, in good agreement with the number quoted by *Koelemeijer et al.* [2003]. A conservative albedo uncertainty of 0.02, is chosen. This accounts for additional interpolation errors from the albedo grid to the GOME pixel location. Furthermore, for regions outside of the 60°N to 60°S band, larger deviations are found between GOME and TOMS. These larger deviations are most likely due to differences in snow and ice cover between the data sets.

[59] A systematic error may occur if the surface albedo climatology predicts a low value for a specific pixel, whereas in reality the pixel is (partly) covered with snow or ice. In such cases however, FRESCO detects an effective surface albedo and surface pressure, so that an intrinsic correction in our algorithm is then thought to occur through our air mass factor computation via equation (13), with $w = 1$ and cloud height z_{cl} replaced by an effective surface height. This recipe, however, does not always work satisfactory, and spurious NO_2 values are sometimes encountered near land-snow boundaries.

[60] We determined the sensitivity $\partial M/\partial a_{sf}$ from the radiative transfer modeling to compute air mass factors for

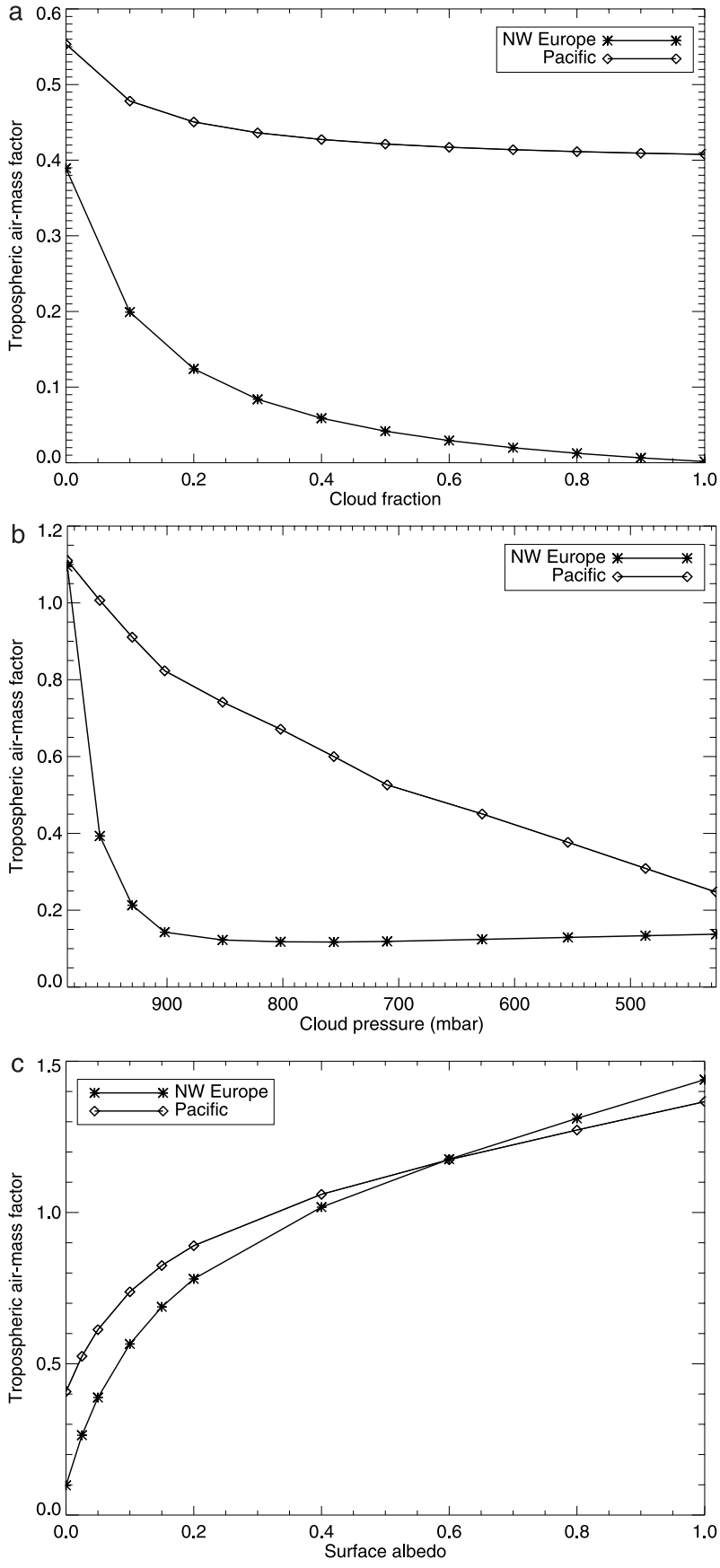
a
NW Europe
Pacific
Tropospheric air-mass factor
Cloud fraction
b
NW Europe
Pacific
Tropospheric air-mass factor
Cloud pressure (mbar)
c
NW Europe
Pacific
Tropospheric air-mass factor
Surface albedo

Figure 5.

the northwest Europe and Pacific pixel. From Figure 5c it can be seen that the impact of the albedo is dependent on the profile shape. The air mass factor sensitivity $\partial M/\partial a_{sf}$ is roughly twice as large for polluted situations as for unpolluted situations for albedos <0.2. The sensitivity is generally largest for albedos in the 0.0–0.2 range. Figure 6c gives an idea of the geographical distribution of the uncertainties due to albedo. For the areas with albedos in March as low as 0.04, for instance Mexico City, Houston, and southeast Brazil with enhanced overlaying NO_2 concentrations, uncertainties are largest but generally <50%. Table 4, representing the mean pixel uncertainty due to albedo uncertainties for March 1997, demonstrates that the uncertainty depends on the tropospheric NO_2 load.

6.4. Errors Due to Profile Shape

[61] The actual profile shape uncertainty is very difficult to assess because of a lack of measured NO_2 profile data. Here we use a "poor man's approach" and study (1) the profile variability in TM3 (explained below), and compare (2) a well-mixed with an unmixed lower troposphere. We use temporal profile variability in TM3 to describe get a feeling for profile shape variability, and use the comparison between two extreme scenarios to get an idea of errors related to the parametrization of boundary-layer mixing. A rough indication of the effect of profile uncertainty is obtained by adding these two contributions.

$$\langle \epsilon^2_{x_a} \rangle = \langle \epsilon^2_{x_{a,tm3}} \rangle + \langle \epsilon^2_{x_{a,mix}} \rangle \tag{16}$$

The first term on the right-hand side in equation (16) is expressed as

$$\langle \epsilon^2_{x_{a,tm3}} \rangle = \sum_{j,k=1}^{n} \frac{\partial M_{tr}}{\partial x_a(z_j)} \frac{\partial M}{\partial x_a(z_k)} S_{jk} \tag{17}$$

where the partial derivatives $\partial M/[\partial x_a(z_j)]$ are the proportionality constants that indicate the change of the air mass factor due to a change in the NO_2 subcolumn at altitude z_j. **S** is the covariance matrix of TM3 profile variability around the monthly mean. For the cloudy part of the pixel, $\partial M/[\partial x_a(z_j)] = 0$ for levels below the cloud. The sensitivity to changes in the NO_2 subcolumn at z_j can be derived from equation (2) and has the following simple form:

$$\frac{\partial M}{\partial x_a(z_j)} = \frac{\sum_{j=1}^{n} x_a(z_j) \cdot [m(z_k) - m(z_j)]}{\sum_{j=1}^{n} x_a(z_j)} = \frac{m(z_j) - M}{x_a} \tag{18}$$

The profile variability covariance matrix elements $S_{j,k}$ are written out as

$$S_{jk} = \langle (x_{a,j} - \langle x_a \rangle_j)(x_{a,k} - \langle x_a \rangle_k) \rangle \tag{19}$$

and are computed from the 31 daily 10.30 hrs TM3 profiles for March 1997. Variability in TM3 profile shapes is caused by changes in the stability and height of the boundary layer, in wet removal of nitric acid, in deep convection and long-range transport by the wind. All these aspects are time and space dependent. It is assumed that the range of variability in TM3 profiles gives a rough estimate of the range of profile shape errors.

[62] We computed the second term in equation (16) as the average of enhanced and reduced mixing. Enhanced mixing is modeled by uniformly redistributing the NO_2 over an idealized BL and by fixing the BL top at approximately 850 hPa, resulting in generally higher air mass factors, whereas reduced mixing is modeled by placing the BL NO_2 load exclusively in the lowest model layer (top at approximately 980 hPa), resulting in lower air mass factors. The second contribution to equation (16) is simply taken as the mean of the air mass factor change due to the enhanced and reduced mixing scenarios.

[63] Figure 6d summarizes the uncertainty in the tropospheric air mass factor due to profile uncertainties as computed following equation (16). For almost all of the globe, the air mass factor uncertainties due to profile uncertainty are <15%, but for regions with high latitudes and little NO_2, the profile variability may be quite high, and uncertainties can be larger than 50%. Table 4 gives an impression of the overall uncertainty in M_{tr} as a consequence of uncertainties in the profile shape. The table illustrates that the air mass factor uncertainties due to profile uncertainty are approximately 10%.

[64] The above results are a first, but clearly only approximate attempt to quantify errors related to profile uncertainties. We note that much larger errors may occur when large emissions are observed at a location where the model predicts only background concentrations (or vice versa). This is the main motivation to involve a model: Most locations of emissions (cities, industry) are well known and included in the emission inventories. One issue is the ability of the TM3 (5° × 3.75°) profile to represent a GOME pixel (320 km × 40 km) profile. TM3 undersamples the GOME pixel size roughly with a factor of 10 (3.75° latitude × 5.00° longitude TM3 grid box corresponds to 400 × 400 km^2 at midlatitudes). Improving the TM3 spatial resolution to 2.5° × 2.5° degrees (275 × 200 km^2) roughly reduces the undersampling factor from 10 to 5. For certain isolated regions such as Florida or Riyadh we find considerable differences in the retrievals with these different horizontal resolutions.

6.5. Errors Due to Aerosols

[65] The exact sensitivity of the tropospheric air mass factor to aerosols depends on a multitude of aerosol parameters: the size distribution, refractive index shape, loading and vertical distribution of the particles. The effect of aerosols on air mass factors is investigated for cloud-free

Figure 5. Sensitivity of the air mass factor to (a) cloud fraction, (b) cloud pressure, and (c) surface albedo for two cases: one above the Pacific (diamonds) and one above northwest Europe (asterisks). In Figure 5a, the cloud pressure is 600 mbar, and surface albedo is 0.05 for northwest Europe and 0.03 for the Pacific. In Figure 5b the cloud fraction is 0.2, and Figure 5c is cloud-free. The y-axis is normalized so that the geometrical air mass factor for these scenarios (2.57) corresponds to 1.0.

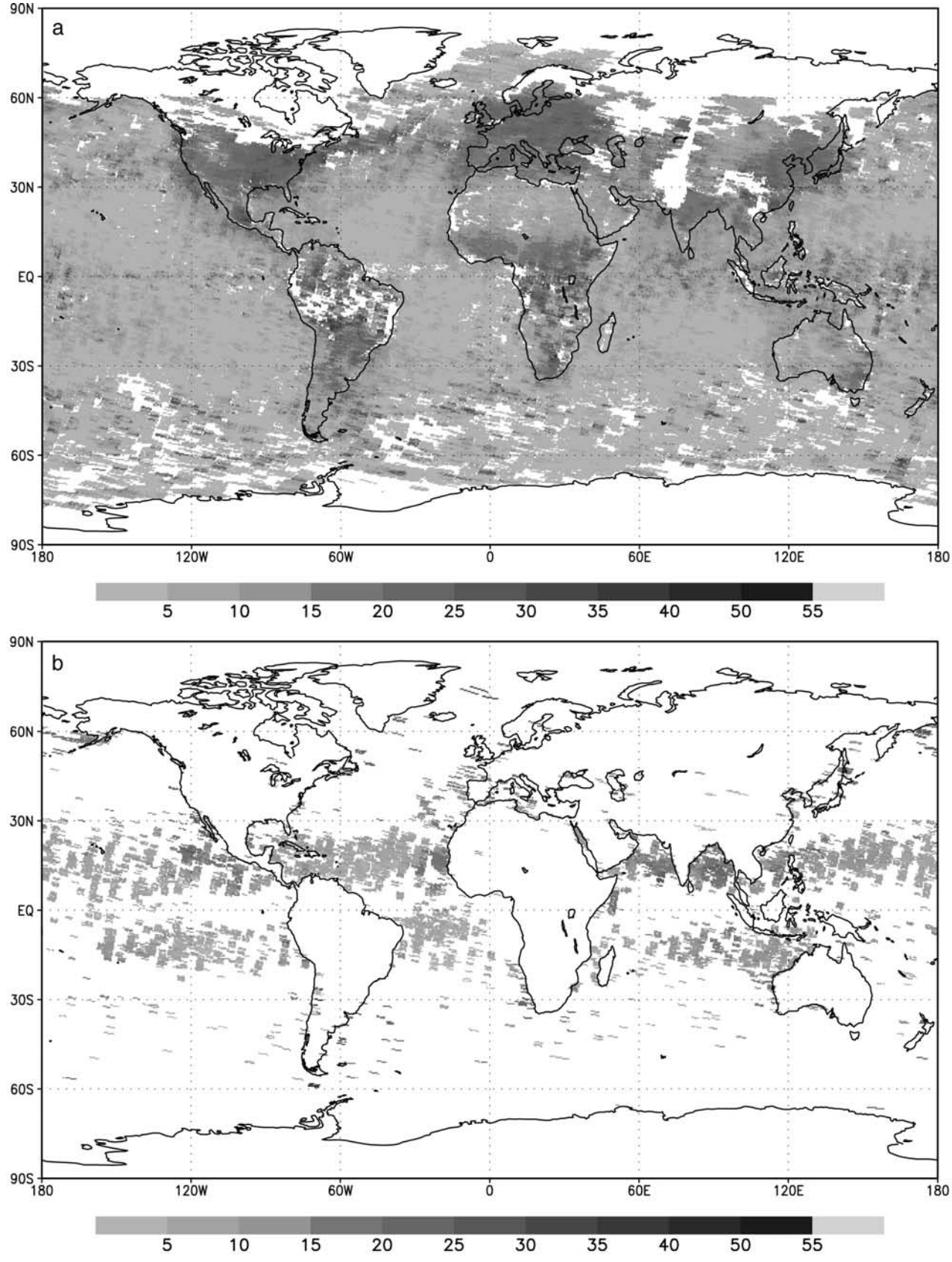

Figure 6. Uncertainty (%) in the tropospheric air mass factor for March 1997 due to uncertainties in the (a) cloud fraction, (b) cloud pressure, (c) surface albedo, and (d) profile shape. Only pixels with a cloud radiance fraction <50% were taken. In Figure 6b only pixels with a cloud pressure >800 hPa were taken. See color version of this figure at back of this issue.

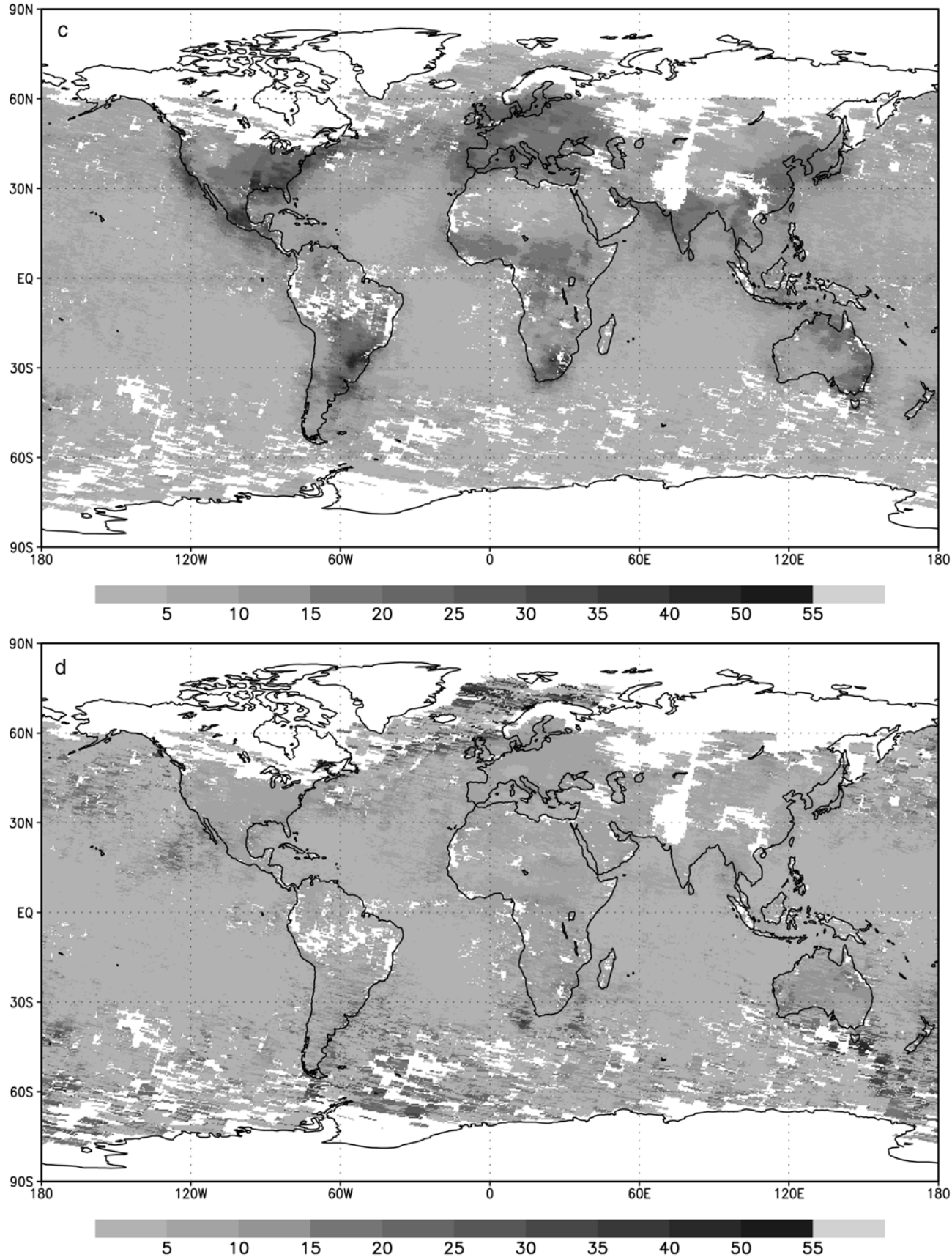

Figure 6. (continued)

Table 4. Mean Uncertainty Tropospheric Air Mass Factor Due to Model Parameters

Type	$N_{\hat{x}_{tr}}$	$\sigma_{M_{tr}}(f_{cl})$	$\sigma_{M_{tr}}(z_{cl})$	$\sigma_{M_{tr}}(a_{sf})$	$\sigma_{M_{tr}}(\mathbf{x_a})$
Clean	$<0.3 \times 0^{15}$ molec. cm^{-2}	5%	2%	5%	10%
Polluted	$0.3-1.0 \times 10^{15}$ molec. cm^{-2}	8%	3%	8%	11%
Heavily polluted	$>1.0 \times 0^{15}$ molec. cm^{-2}	15%	2%	15%	9%

atmospheres by comparing air mass factors computed with DAK with and without aerosols.

[66] The following four general aerosol types were considered: (1) urban-industrial aerosol from fossil fuel combustion in populated industrial regions, (2) biomass burning aerosols produced by forest and grassland fires, (3) desert dust, and (4) aerosol of marine origin. The aerosol properties were taken from microphysical aerosol models proposed by *Torres et al.* [2002], which are considered representative for aerosol mixtures over regions with the size of a moderate resolution satellite pixel, and are summarized in Table 5. All aerosol types have single scattering albedo ω_0 larger than 0.88, consistent with numbers taken from a recent paper of *Dubovik et al.* [2002], who summarize 8 years of worldwide distributed data from the AERONET network, and report 0.88 (at 440 nm) as smallest value (for African savannah biomass burning aerosol) in their ω_0.

[67] A tropospheric air mass factor aerosol correction factor is defined as the ratio of the air mass factor with and without aerosols present. The air mass factors are computed for a fixed aerosol vertical distribution (an exponentially decreasing shape with a scale height of 2 km, also taken from *Torres et al.* [2002]) and aerosol optical thicknesses between 0.0 and 1.0, and an albedo of 0.05. Figure 8 shows the effect of the four types of aerosols on the air mass factor. The aerosol correction factors lie in the 1.0–1.4 range for aerosol optical thicknesses up to 1.0. Contrary to our findings, *Martin et al.* [2003] report correction factors <1.0. This is likely due to their microphysical aerosol model that attributes more importance to absorption. For instance they use $\omega_0 = 0.75$ for dust, whereas in this work $\omega_0 = 0.89$ is used, consistent with *Dubovik et al.* [2002].

[68] It is crucial to realize that the TOA reflectance input to cloud retrieval schemes is modified by the presence of aerosols. Cloud algorithms typically do not account for aerosols, and overestimate cloud fraction and underestimate cloud top altitude values when a low atmospheric aerosol layer is added to a pure Rayleigh atmosphere. A higher cloud fraction can be understood from the excess TOA reflectance caused by the additional scattering due to aerosols. An underestimated cloud height is a consequence of the multiple scattering enhanced light path due to the aerosol layer.

[69] The increased cloud fraction and decreased cloud height tend to increase the light path through the troposphere and hence increase the tropospheric air mass factor. The neglect of aerosols in the air mass factor calculation is therefore thought to be partly compensated by the indirect effect of aerosols on the cloud retrieval scheme. This assumption was investigated by carrying out a study of the sensitivity of the O_2-O_2 cloud retrieval algorithm developed for OMI to aerosol optical thickness [*Acarreta and de Haan*, 2002]. The results of these tests are collected in Table 6 for $\tau_{aer} = 1.0$. The change in cloud fraction is smaller than the expected precision of the cloud algorithm (±0.05), but the change in cloud pressure seems to be significant (more than the expected precision of ±50 hPa). The table shows that the cloud algorithm is less sensitive

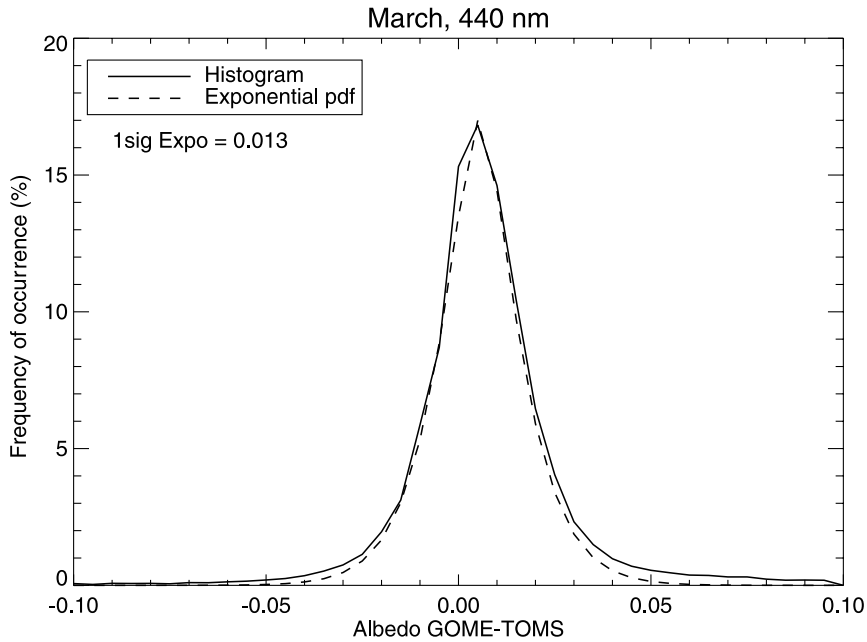

Figure 7. Histogram of the difference between the GOME and TOMS constructed surface albedos at 440 nm in March, for latitudes between 60°N and 60°S.

Table 5. Aerosol Type Parameters[a]

	Mean Radius, μm		Std. Dev., μm		Refractive Index			
Type	m1	m2	m1	m2	Re	Im	Fraction of m2	ω_0
Industrial	0.088	0.509	1.499	2.160	1.400	0.004	4.04×10^{-4}	0.964
Biomass burning	0.087	0.567	1.537	2.203	1.500	0.001	2.06×10^{-4}	0.88
Desert dust	0.052	0.67	1.697	1.806	1.530	2.58×10^{-3}	4.35×10^{-3}	0.89
Oceanic	0.240	2.000	2.030	2.030	1.390	5×10^{-8}	1.41×10^{-4}	1.000

[a]All types have a bimodal distribution. The mean particle radius and its standard deviation are given for both modes (m1 and m2). The relative fraction of the second mode to the number concentration is given by the fraction of m2. All aerosol parameters are computed at 436.5 nm. Std. Dev., standard deviation.

to biomass burning and dust aerosol than to industrial aerosol because of the stronger absorbing nature of the former aerosol types. Tropospheric air mass factors are subsequently calculated through our retrieval scheme by using cloud fractions and cloud heights which implicitly also account for aerosols. We used the adjusted cloud fractions and pressures as given in Table 6. The results are compared with the theoretical radiative transfer calculations described above.

[70] We picked only pixels with model parameters similar to those chosen in the radiative transfer study (albedo = 0.05, cloud-free pixels, same solar and viewing zenith angles) to ensure consistency with our radiative transfer results depicted in Figure 8. A comparison of the expected aerosol correction factor versus the actual correction effect through the modified cloud fraction and height is shown in Figure 9. Even for large values of τ_{aer}, the radiative transfer aerosol correction factor and the actual retrieval cloud correction factor agree to within 10%. This comparison suggests that cloud algorithms implicitly correct for aerosol through their modified cloud fraction and height. A comparison for other solar zenith angles showed agreement to within 15%.

[71] This sensitivity study is performed with the OMI O_2-O_2 algorithm (470 nm) rather than with the FRESCO algorithm (770 nm). The latter is roughly half as sensitive to light scattered by aerosols as the OMI cloud algorithm, since a typical ratio $\tau_{aer}(770)$: $\tau_{aer}(470)$ of 1:2 is estimated from Ångström's relation. On the other hand, cloud heights are expected to be well retrieved by FRESCO because of the stronger O_2-A relative to the O_2-O_2 absorption feature. However, since both algorithms are based on the same set of principles we expect a similar cancellation.

[72] The main conclusion of this subsection is that correcting air mass factors for aerosols can not be decoupled from correcting cloud retrieval schemes for aerosols. These corrections have a comparable impact on the air mass factor, and both corrections nearly cancel. *Martin et al.* [2003] suggested that NO_2 retrievals can be improved upon by directly accounting for aerosols, but we question their approach, since they did not take into account the sensitivity of their cloud retrieval algorithm [*Kurosu et al.*, 1999] to aerosol.

6.6. Summary of Tropospheric Air Mass Factor Errors

[73] The previous sections focused on the individual errors in the air mass factor due to uncertainties in cloud parameters, surface albedo and profile shape. Appendix A discusses the correlations between the errors in these air

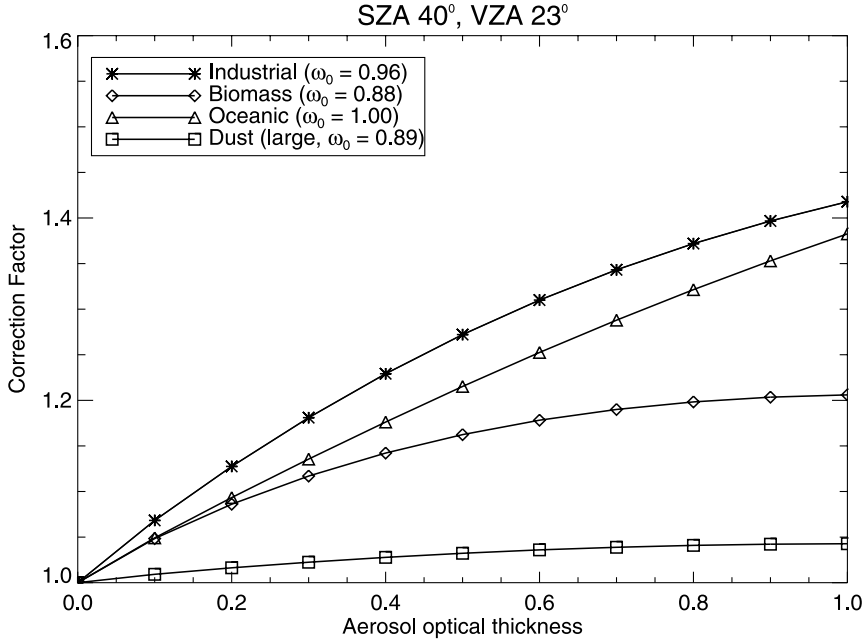

Figure 8. Air mass factor aerosol correction factors (relative to clear sky without aerosols) computed with DAK as a function of aerosol optical thickness for solar zenith angle 40°, viewing angle 23°, and surface albedo 0.05.

Table 6. Change in Cloud Fraction and Cloud Pressure Due to Aerosol Optical Thickness of 1.0

Type	δf_{cl}	δz_{cl}
Industrial	+0.013	+314 hPa
Biomass burning	+0.004	+76 hPa
Dust	0.0	−25 hPa

mass factor input parameters. On the basis of our findings in Appendix A, we can write out equation (12) taking into account the nonzero covariance terms. This leads to the following expression, where we have omitted the aerosol term because of reasons mentioned in section 6.5

$$\langle \epsilon_{M_{tr}}^2 \rangle = \left(K_{f_{cl}} \sigma_{f_{cl}}\right)^2 \left(K_{z_{cl}} \sigma_{z_{cl}}\right)^2 + \left(K_{a_{sf}} \sigma_{a_{sf}}\right)^2 + \left(K_{\mathrm{x_{a,tr}}} \sigma_{\mathrm{x_{a,tr}}}\right)^2 + 2\left(K_{f_{cl}} K_{a_{sf}} \langle \epsilon_{f_{cl}} \epsilon_{a_{sf}} \rangle\right) \quad (20)$$

Figure 10 shows the geographical distribution of the average uncertainty computed with equation (20). The uncertainty of M_{tr} is largest in areas with largest NO_2 emissions. Especially regions with a low surface albedo (in March), such as Mexico City, and the Houston and Johannesburg areas, are very sensitive to albedo uncertainties, and this is reflected in uncertainty values of more than 50%. The uncertainty in the air mass factor may also be particularly high over outflow regions, such as west of California, off the U.S. East Coast, over the North and the East Sea, and to a lesser extent west of the West African coast and between China and Japan. The contribution of profile uncertainties to the total air mass factor uncertainty is largest over some unexpected oceanic regions with apparently strong profile variability (for instance, southeast of Australia and South America), however, these regions have little tropospheric NO_2 and are therefore of less interest.

[74] The first column in Table 7 gives the average uncertainty for all pixels with cloud radiance fractions <0.5 in March 1997, for the clean, moderately and heavily polluted regimes. From the table we see that the uncertainty is related to the regime, with the largest uncertainty for the most polluted pixels.

7. Total Uncertainty in Tropospheric NO_2 Columns

[75] Figures 11 and 12 show the monthly mean retrieved tropospheric NO_2 columns (H. J. Eskes and K. F. Boersma, manuscript in preparation, 2004) and their absolute relative uncertainty from equation (5) and equation (20) for March 1997.

[76] Most striking in Figure 12 is the difference in error budget between the "clean" and "polluted" areas. Over the oceans and the remote continental regions, the overall tropospheric retrieval uncertainty is dominated by errors in the spectral fitting and the stratospheric column estimate. For larger columns over continental areas, the relative uncertainty in the retrieved column reduces to 35–60%, and is dominated by the uncertainty in the tropospheric air mass factor. Retrieval results are generally best for regions with strong NO_2 sources (California, northwest Europe, Japan) and/or high surface albedos (Saudi desert).

[77] Table 7 summarizes the mean uncertainties in tropospheric columns for different retrieval scenarios. Obviously, the relative uncertainty in clean areas ($<0.3 \times 10^{15}$ molec. cm^{-2}) indicates that such small values have generally little meaning. However, moderate values (between 0.3 and 1.0×10^{15} molec. cm^{-2}) are detectable, given their, on

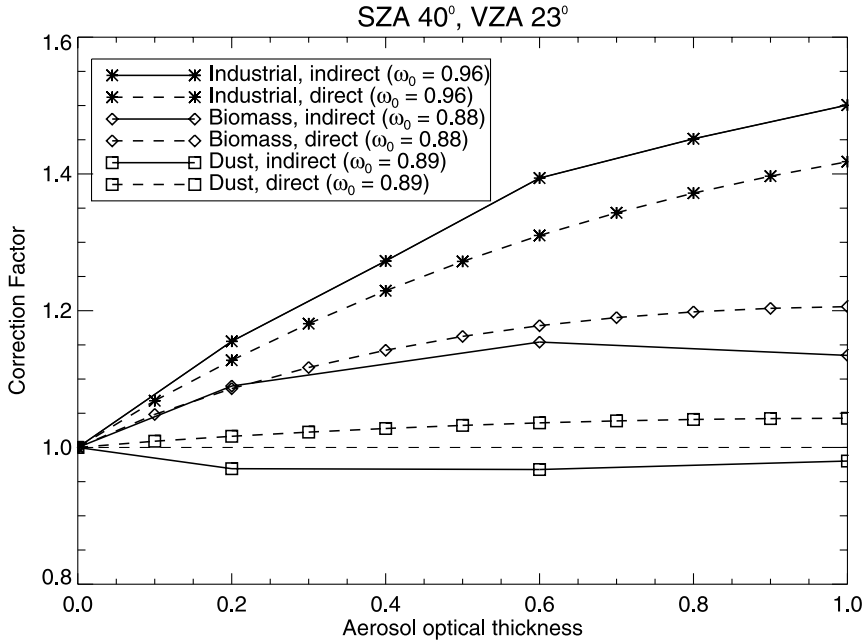

Figure 9. The solid lines show the indirect air mass factor correction factors resulting from the aerosol-modified cloud fraction and height. The dashed lines are as in Figure 8 and show the direct radiative transfer calculations.

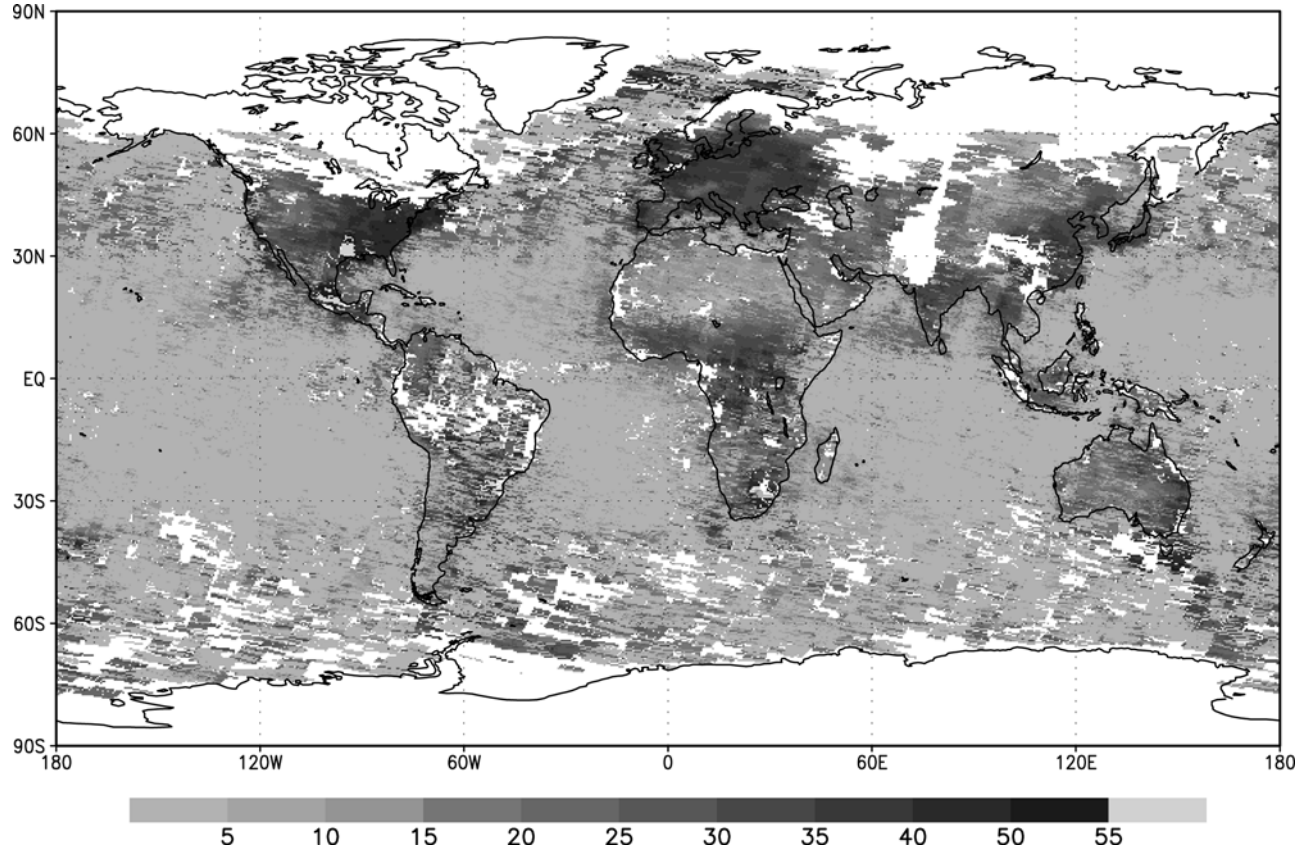

Figure 10. Uncertainty (%) in the tropospheric air mass factor for March 1997 due to uncertainties in the cloud fraction, cloud height, surface albedo and profile shape. Only pixels with a cloud radiance fraction <0.5 were taken. See color version of this figure at back of this issue.

average, better than 100% uncertainty. Best results are obtained for tropospheric columns $>1.0 \times 10^{15}$ molec. cm^{-2}) with an average uncertainty better than 50%.

8. Conclusions and Outlook

[78] If a significant tropospheric slant column density is retrieved, a meaningful estimate of the tropospheric vertical column can be given with a precision of 35–60%. These retrieval uncertainties are dominated by the uncertainty in the estimate of the tropospheric air mass factor. The most important uncertainties associated with the computation of the tropospheric air mass factor are cloud fraction, surface albedo and profile shape. Estimated uncertainties in the cloud height of 50 hPa do not significantly influence our results.

[79] We conclude that an explicit aerosol correction procedure is complicated, since cloud algorithms are sensitive to aerosols and tend to slightly overestimate cloud fraction and underestimate cloud height, and subsequent incorporation of the modified cloud parameters in the algorithm is indirectly accounting for aerosol effects in the retrieval procedure.

[80] One aspect that needs to be accounted for is the temperature-dependence of the NO_2 cross section. Not accounting for the effective NO_2 temperature leads to structurally underestimating slant columns in polluted areas by up to 20% because of warmer boundary layer NO_2, and incidentally overestimating slant columns in clean regions where the stratosphere is colder than usual ($T \ll 220$ K).

[81] DOAS tropospheric NO_2 retrievals can be improved upon in many ways. Important issues in future research are the improvement of slant column density fitting by resolving the diffuser plate problems, and by properly accounting for Raman scattering in the spectral fitting as well as in the air mass factor calculations. However, errors related to the slant column fitting are small compared with the other error sources. Estimating the stratospheric field can be done more accurately. The current assumption of zonal invariant stratospheric NO_2 causes problems in the winter hemisphere when strong dynamic activity causes zonal variability. Data assimilation of measurements in a CTM has the potential of improving this issue.

[82] The uncertainty in the tropospheric air mass factor will be reduced, when the following model parameter estimates are improved: (1) High-quality albedo maps at high spatial resolution. Current (MODIS and

Table 7. Mean Uncertainty Tropospheric Air Mass Factor and Column

Type	$\sigma_{M_{tr}}$	$\sigma_{N_{v,tr}}$
Clean	17%	>100%
Polluted	20%	55–125%
Heavily polluted	29%	35–60%

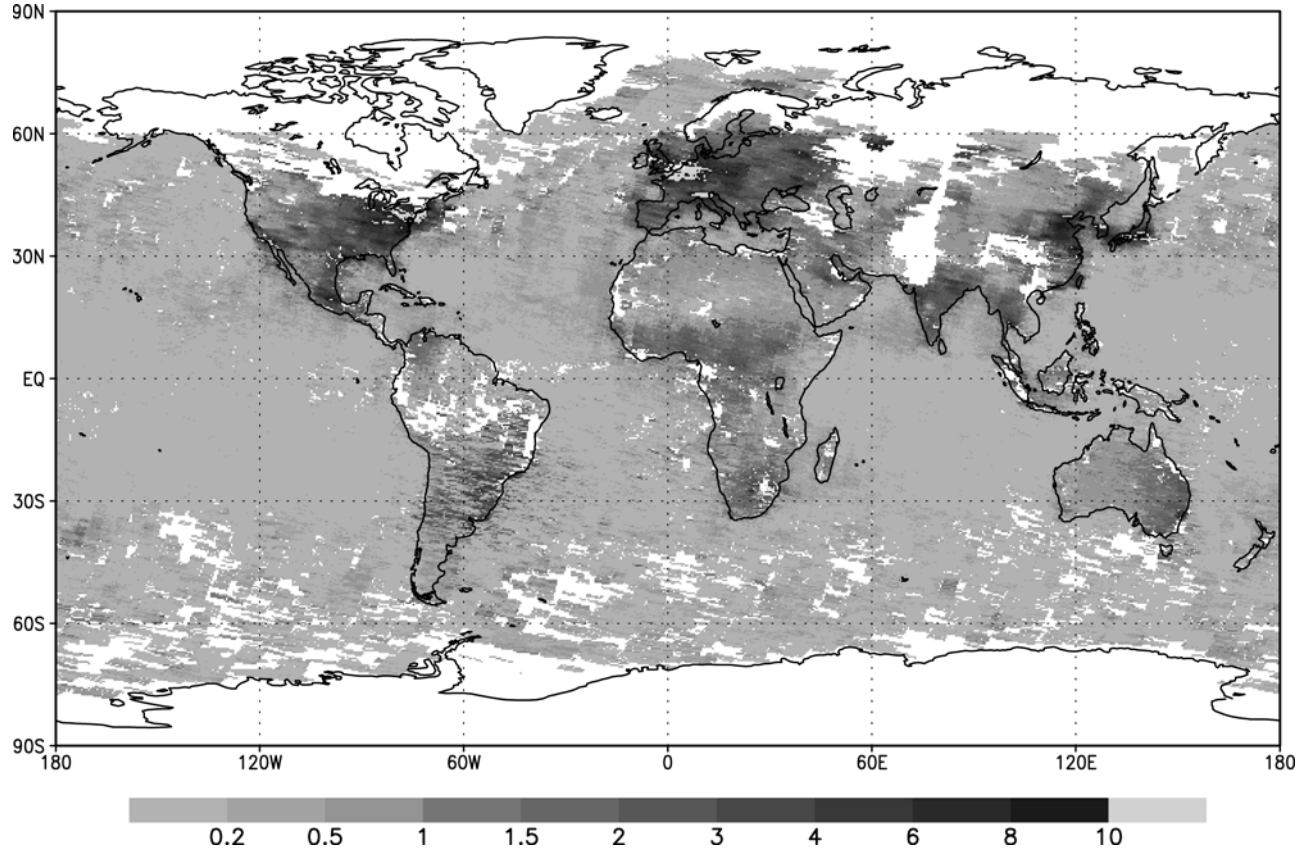

Figure 11. Monthly mean tropospheric columns for March 1997. Only pixels with a cloud radiance fraction <0.5 were taken. See color version of this figure at back of this issue.

SCIAMACHY) and new (OMI) instruments have the potential to generate well-resolved high-quality albedo maps, and these will be essential in reducing the uncertainty of tropospheric retrievals. (2) Better cloud retrievals, especially for small cloud fractions. It is important that the development and validation of improved cloud retrieval schemes continues, especially for low cloud fractions. (3) Improved (validated) tropospheric profile shapes. Profile shape errors may be reduced by improving the spatial resolution of the CTM. However, a clear need exists to validate tropospheric profile shapes, since the assumed profiles have the potential of systematically biasing retrieval results. (4) A better understanding of the way aerosols influence the air mass factor and cloud retrievals.

[83] Finally, a thorough validation campaign of tropospheric NO_2 profiles and columns over polluted regions is essential. Profile and column measurements of NO_2 in the polluted troposphere are sparse, important for validation and algorithm improvement, and therefore such measurements are greatly encouraged.

Appendix A: Covariance Terms

[84] In this section we investigate any dependencies between the air mass factor input parameters. If uncertainties in the input parameters i and j are uncorrelated, σ_{ij}^2 (with $i \neq j$) vanishes.

[85] Cloud retrieval algorithms employ the absolute radiance level at the satellite detector to determine f_{cl}, and the depth of a specific absorption (O_2-A or O_2-O_2) band to determine z_{cl}. If the depth of the absorption band is attributed to an incorrect cloud fraction this will result in an erroneous cloud height, and hence $\langle \epsilon_{f_{cl}} \epsilon_{z_{cl}} \rangle$ is not zero. However, since the uncertainties in the air mass factor due to cloud height uncertainties are small (<3%), the correlations with this parameter is neglected.

[86] Cloud fractions are sensitive to surface albedo, especially for small cloud fractions and a high surface albedo. *Koelemeijer et al.* [2001] determined the dependence of the uncertainty in the cloud fraction on the albedo uncertainty to be

$$\sigma_{f_{cl}} = -\frac{1 - f_{cl}}{a_c - a_{sf}} \sigma_{a_{sf}} \tag{A1}$$

with a_c the cloud albedo. The correlation coefficient is

$$\langle \epsilon_{f_{cl}} \epsilon_{a_{sf}} \rangle = -\frac{1 - f_{cl}}{a_c - a_{sf}} \frac{\sigma_{a_{sf}}}{\sigma_{f_{cl}}} \tag{A2}$$

When cloud fractions are small, cloud height uncertainties caused by albedo uncertainties become large. A surface albedo uncertainty of 0.02 gives rise to uncertainties in cloud heights of up to more than 150 hPa for a cloud fractions of 5%. We therefore conclude that the uncertainties in $\epsilon_{a_{sf}}$ and $\epsilon_{z_{cl}}$ are correlated. Again, this correlation is neglected because the uncertainties in the air mass factor due to cloud height uncertainties are small.

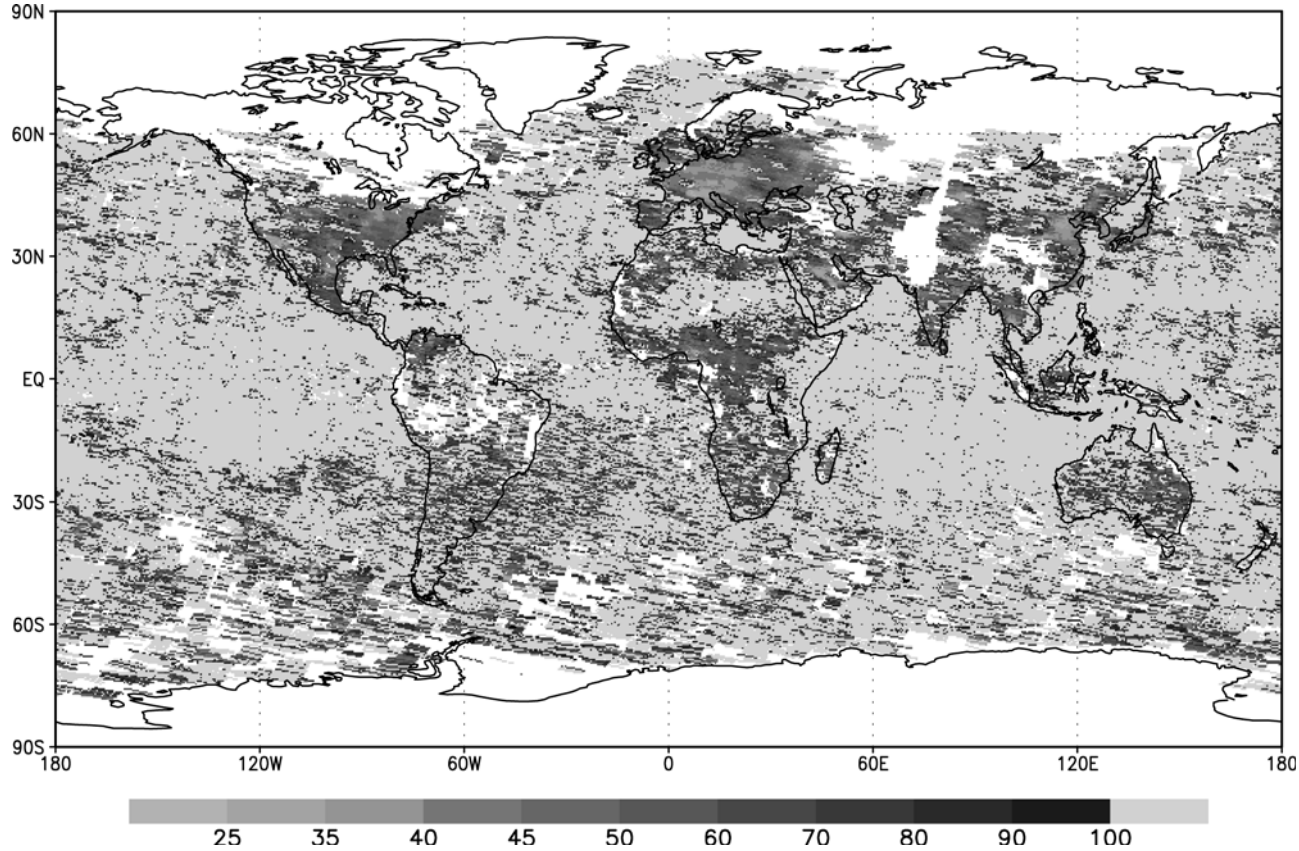

Figure 12. Relative uncertainty in tropospheric columns for March 1997. Only pixels with a cloud radiance fraction <0.5 were taken. See color version of this figure at back of this issue.

[87] Errors in the NO_2 profile shape and other input parameters are not related in any way, since these quantities are determined in a completely independent way (f_{cl} and z_{cl} from the cloud algorithm, a_{sf} from the surface albedo climatology and $\mathbf{x_a}$ from a chemical-transport model) so that $\langle \epsilon_{\mathbf{x_a}} \epsilon_j \rangle = 0$.

[88] **Acknowledgments.** The authors acknowledge Pepijn Veefkind for computation of the altitude-dependent air mass factors and Juan R. Acarreta for computation of the effect of aerosols on the cloud retrieval procedure. Steffen Beirle is kindly acknowledged for the provision of the slant column data. Stimulating discussions with Pepijn Veefkind, Juan R. Acarreta, Johan de Haan, and Michiel van Weele have contributed to this work. This work is supported by the European Union GOA project (contract EVK2-CT-2000-00062).

References

Acarreta, J. R., and J. F. de Haan (2002), Cloud pressure algorithm based on O_2-O_2 absorption, in *OMI Algorithm Theoretical Basis Document*, vol. 3, *Clouds, Aerosols and Surface UV Irradiance*, *ATBD-OMI-03, Version 2.0*, edited by P. Stammes and R. Noordhoek, pp. 9–30, NASA Distrib. Active Arch. Cent., Greenbelt, Md., Aug.

Balis, D. S., C. Zerefos, A. Tsiropoulou, P. Taalas, and A. Anthis (2001), Validation of GOME total ozone using ground-based total ozone measurements from the WMO Global Atmosphere Watch, paper presented at SAF Training Workshop, Eur. Organ. for the Exploit. of Meteorol. Satell., Halkidiki, Greece.

Boersma, K. F., E. J. Bucsela, E. J. Brinksma, and J. F. Gleason (2002), NO_2, in *OMI Algorithm Theoretical Basis Document*, vol. 4, *OMI Trace Gas Algorithms*, *ATBD-OMI-04, Version 2.0*, edited by K. Chance, pp. 13–36, NASA Distrib. Active Arch. Cent., Greenbelt, Md., Aug.

Burrows, J. P., A. Dehn, B. Deters, S. Himmelmann, A. Richter, S. Voigt, and J. Orphal (1998), Atmospheric remote-sensing reference data from GOME: Part 1. Temperature-dependent absorption cross-section of NO_2 in the 231–794 nm range, *J. Quant. Spectrosc. Radiat. Transfer*, *60*, 1025–1031.

Burrows, J. P., et al. (1999), The Global Ozone Monitoring Exeriment (GOME): Mission concept and first scientific results, *J. Atmos. Sci.*, *56*, 151–175.

Chance, K., P. Palmer, R. J. D. Spurr, R. V. Martin, T. P. Kurosu, and D. J. Jacob (2000), Satellite observations of formaldehyde over North America from GOME, *Geophys. Res. Lett.*, *27*, 3461–3464.

de Haan, J. F., P. B. Bosma, and J. W. Hovenier (1987), The adding method for multiple scattering calculations of polarized light, *Astron. Astrophys.*, *183*, 371–391.

Dentener, F. J., and P. J. Crutzen (1994), A global 3D model of the ammonia cycle, *J. Atmos. Chem.*, *19*, 331–369.

Dentener, F., M. van Weele, M. Krol, S. Houweling, and P. van Velthoven (2002), Trends and inter-annual variability of methane emissions derived from 1979–1993 global CTM simulations, *Atmos. Chem. Phys. Discuss.*, *2*, 249–287.

Dubovik, O., B. Holben, T. F. Eck, A. Smirnov, Y. J. Kaufman, M. D. King, D. Tanré, and I. Slutsker (2002), Variability of absorption and optical properties of key aerosol types observed in worldwide locations, *J. Atmos. Sci.*, *59*, 590–608.

Eisinger, M., and J. P. Burrows (1998), Tropospheric sulfur dioxide observed by the ERS-2 GOME instrument, *Geophys. Res. Lett.*, *25*, 4177–4180.

Eskes, H. J., and K. F. Boersma (2003), Averaging kernels for DOAS total-column satellite retrievals, *Atmos. Chem. Phys.*, *3*, 1285–1291.

Eskes, H. J., et al. (2003), Combined retrieval, modeling and assimilation approach to GOME NO_2, in *GOA Final Report*, *European Commission Fifth Framework Programme 1998–2002*, *EESD-ENV-99-2*, pp. 116–122, Eur. Comm., De Bilt, Netherlands, April.

Guelle, W., Y. J. Balkanski, M. Schulz, F. Dulac, and P. Monfray (1998), Wet deposition in a global size-dependent aerosol transport model: 1. Comparison of a 1 year Pb^{210} simulation with ground measurements, *J. Geophys. Res.*, *103*, 11,429–11,445.

Herman, J. R., and E. A. Celarier (1997), Earth surface reflectivity climatology at 340–380 nm from TOMS data, *J. Geophys. Res.*, *102*, 28,003–28,011.

Knudsen, B. M. (2003), On the accuracy of analysed low temperatures in the stratosphere, *Atmos. Chem. Phys. Discuss.*, *3*, 4411–4429.

Koelemeijer, R. B. A., P. Stammes, J. W. Hovenier, and J. F. de Haan (2001), A fast method for retrieval of cloud parameters using oxygen A-band measurements from Global Ozone Monitoring Experiment, *J. Geophys. Res.*, *106*, 3475–3490.

Koelemeijer, R. B. A., J. F. de Haan, and P. Stammes (2003), A database of spectral surface reflectivity in the range 335–772 nm derived from 5.5 years of GOME observations, *J. Geophys. Res.*, *108*(D2), 4070, doi:10.1029/2002JD002429.

Kurosu, T. P., K. Chance, and R. J. D. Spurr (1999), CRAG: Cloud Retrieval Algorithm for the European Space Agency's Global Ozone Monitoring Experiment, in *ESAMS '99: European Symposium of Atmospheric Measurements From Space*, vol. 2, pp. 513–521, Eur. Space Agency, Noordwijk, Netherlands.

Lauer, A., M. Dameris, A. Richter, and J. P. Burrows (2002), Tropospheric NO_2 columns: A comparison between model and retrieved data from GOME measurements, *Atmos. Chem. Phys.*, *2*, 67–78.

Leue, C., M. Wenig, T. Wagner, O. Klimm, U. Platt, and B. Jähne (2001), Quantitative analysis of NO_x emissions from Global Ozone Monitoring Experiment satellite image sequences, *J. Geophys. Res.*, *106*, 5493–5505.

Louis, J. F. (1979), A parametric model of vertical eddy fluxes in the atmosphere, *Boundary Layer Meteorol.*, *17*, 187–202.

Marland, G., T. A. Boden, and R. J. Andres (2000), CO_2 emission trends: A compendium of data on global change, technical report, Carbon Dioxide Anal. Cent., Oak Ridge Natl. Lab., Oak Ridge, Tenn.

Martin, R. V., et al. (2002), An improved retrieval of tropospheric nitrogen dioxide from GOME, *J. Geophys. Res.*, *107*(D20), 4437, doi:10.1029/2001JD001027.

Martin, R. V., D. J. Jacob, K. Chance, T. P. Kurosu, P. I. Palmer, and M. J. Evans (2003), Global inventory of nitrogen oxide emissions constrained by space-based observations of NO_2 columns, *J. Geophys. Res.*, *108*(D17), 4537, doi:10.1029/2003JD003453.

Meijer, E., P. van Velthoven, D. Brunner, H. Huntrieser, and H. Kelder (2001), Improvement and evaluation for the parameterisation of nitrogen oxide production by lightning, *Phys. Chem. Earth, Part C: Sol.-Terr. Planet. Sci.*, *26*, 577–583.

Palmer, P. I., D. J. Jacob, K. Chance, R. V. Martin, R. J. D. Spurr, T. P. Kurosu, I. Bey, R. Yantosca, A. Fiore, and Q. Li (2001), Air-mass factor formulation for spectroscopic measurements from satellites: Application to formaldehyde retrievals from GOME, *J. Geophys. Res.*, *106*, 14,539–14,550.

Platt, U. (1994), Differential Optical Absorption Spectroscopy (DOAS), in *Air Monitoring by Spectroscopic Techniques*, *Chem. Anal.*, vol. 127, edited by M. W. Sigrist, pp. 27–76, Wiley-Interscience, Hoboken, N. J.

Prather, M., et al. (2001), Atmospheric chemistry and greenhouse gases, in *Climate Change 2001, the Scientific Basis: Contribution of Working Group I to the Third Assessment Report of the Intergovernmental Panel on Climate Change*, edited by J. T. Houghton et al., chap. 4, pp. 239–287, Cambridge Univ. Press, New York.

Richter, A., and J. P. Burrows (2002), Tropospheric NO_2 from GOME measurements, *Adv. Space Res.*, *29*, 1673–1683.

Richter, A., H. Nüss, B. M. Sinnhuber, T. Wagner, and J. P. Burrows (2002), Quantification of tropospheric measurements from nadir viewing UV/visible instruments, in *The Use and Usability of Satellite Data for Tropospheric Research: TROPOSAT Annual Report 2001*, pp. 59–62, EUROTRAC-2 Int. Sci. Secr., Munich, Germany.

Rodgers, C. D. (2000), *Inverse Methods for Atmospheric Sounding: Theory and Practice*, *Ser. Atmos. Oceanic Planet. Phys.*, vol. 2, World Sci., River Edge, N. J.

Russel, G., and J. Lerner (1981), A new finite difference scheme for the tracer transport equation, *J. Appl. Meteorol.*, *20*, 1483–1498.

Spurr, R., and W. Thomas (2000), DOAS spectral fitting algorithm, in *GOME Level 1 to 2 Algorithm Description*, *Tech. Note ER-TN-DLR-GO-0025*, *Iss./Rev. 2/B*, pp. 18–27, Dtsch. Zent. für Luft- und Raumfahrt, Oberpfaffenhofen, Germany.

Stammes, P., J. F. de Haan, and J. W. Hovenier (1989), The polarized internal radiation field of a planetary atmosphere, *Astron. Astrophys.*, *225*, 239–259.

Torres, O., R. Decae, P. Veefkind, and G. de Leeuw (2002), OMI aerosol retrieval algorithm, in *OMI Algorithm Theoretical Basis Document*, vol. 3, *Clouds, Aerosols and Surface UV Irradiance*, *ATBD-OMI-03, Version 2.0*, edited by P. Stammes and R. Noordhoek, pp. 47–69, NASA Distrib. Active Arch. Cent., Greenbelt, Md., Aug.

Valks, P. J. M., R. B. A. Koelemeijer, M. van Weele, P. van Velthoven, J. P. F. Fortuin, and H. Kelder (2003), Variability in tropical tropospheric ozone: Analysis with Global Ozone Monitoring Experiment observations and a global model, *J. Geophys. Res.*, *108*(D11), 4328, doi:10.1029/2002JD002894.

van Aardenne, J. A., F. J. Dentener, C. G. M. Klein Goldewijk, J. Lelieveld, and J. G. J. Olivier (2001), A high resolution data set of historical anthropogenic trace gas emissions for the period 1890–1990, *Global. Biogeochem. Cycles*, *15*, 909–928.

Vandaele, A. C., C. Hermans, P. C. Simon, M. Carleer, R. Colin, S. Fally, M. F. Merienne, A. Jenouvrier, and B. Coquart (1998), Measurements of the NO_2 absorption cross-section from 42 000 cm^{-1} to 10 000 cm^{-1} (238–1000 nm) at 220 K and 294 K, *J. Quant. Spectrosc. Radiat. Transfer*, *59*, 171–184.

Velders, G. J. M., C. Granier, R. W. Portmann, K. Pfeilsticker, M. Wenig, T. Wagner, U. Platt, A. Richter, and J. P. Burrows (2001), Global tropospheric NO_2 column distributions: Comparing three-dimensional model calculations with GOME measurements, *J. Geophys. Res.*, *106*, 12,643–12,660.

Vermote, E., and D. Tanré (1992), Analytic expressions for radiative properties of planar Rayleigh scattering media, including polarization contributions, *J. Quant. Spectrosc. Radiat. Transfer*, *47*, 305–314.

Wagner, T., and U. Platt (1998), Satellite mapping of enhanced BrO concentrations in the troposphere, *Nature*, *395*, 486–490.

Wagner, T., C. Leue, M. Wenig, and U. Platt (1999), GOME NO_2 validation studies, in *ERS-2 GOME Data Products Delta Characterisation Report 1999*, edited by J.-C. Lambert and P. Skarlas, pp. 87–96, Eur. Space Res. Inst., Frascati, Italy.

Wenig, M. (2002), Satellite measurements of long-term global tropospheric trace gas distributions and source strengths, Ph.D. thesis, Heidelberg Univ., Heidelberg, Germany.

K. F. Boersma, E. J. Brinksma, and H. J. Eskes, Royal Netherlands Meteorological Institute, P. O. Box 201, 3730 AE De Bilt, Netherlands. (boersma@knmi.nl; brinksma@knmi.nl; eskes@knmi.nl)

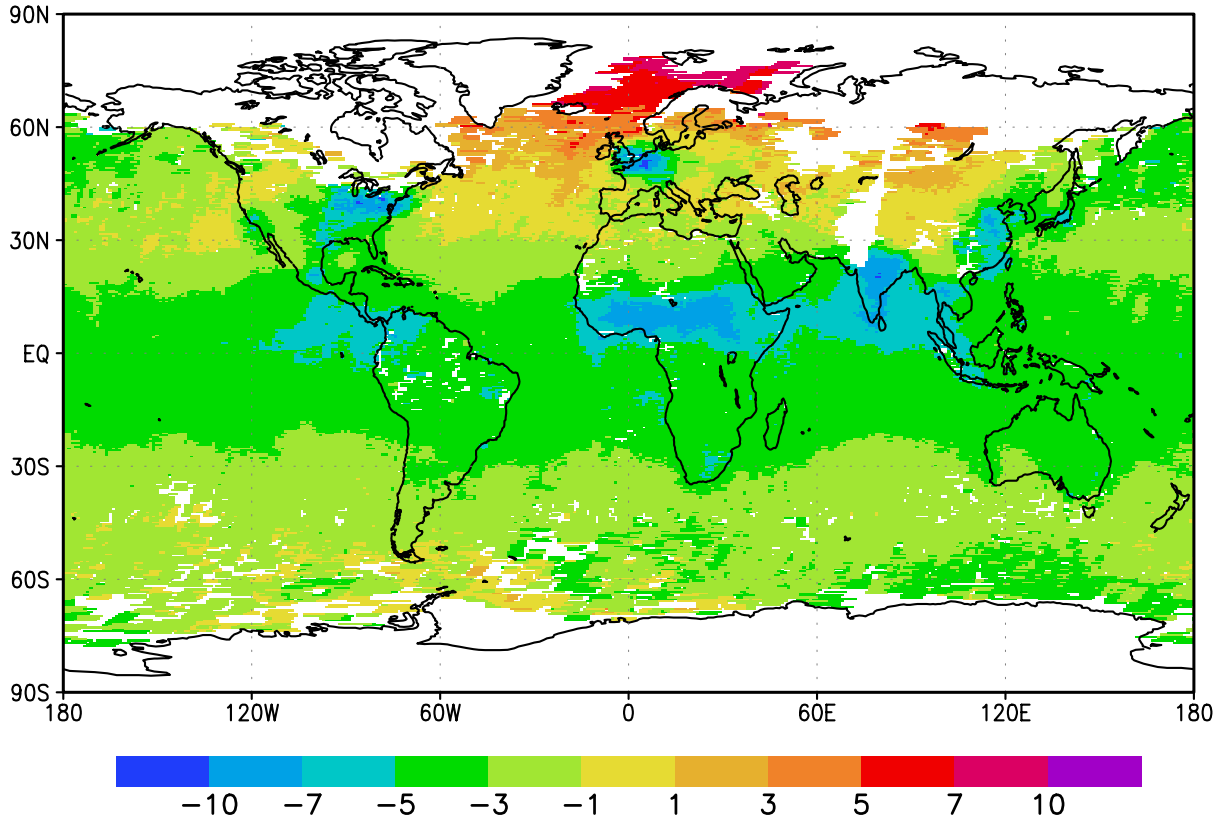

Figure 3. Systematic effect (%) of not accounting for atmospheric temperature variations in slant column retrieval for March 1997. Only pixels with a cloud radiance fraction smaller than 0.5 were taken.

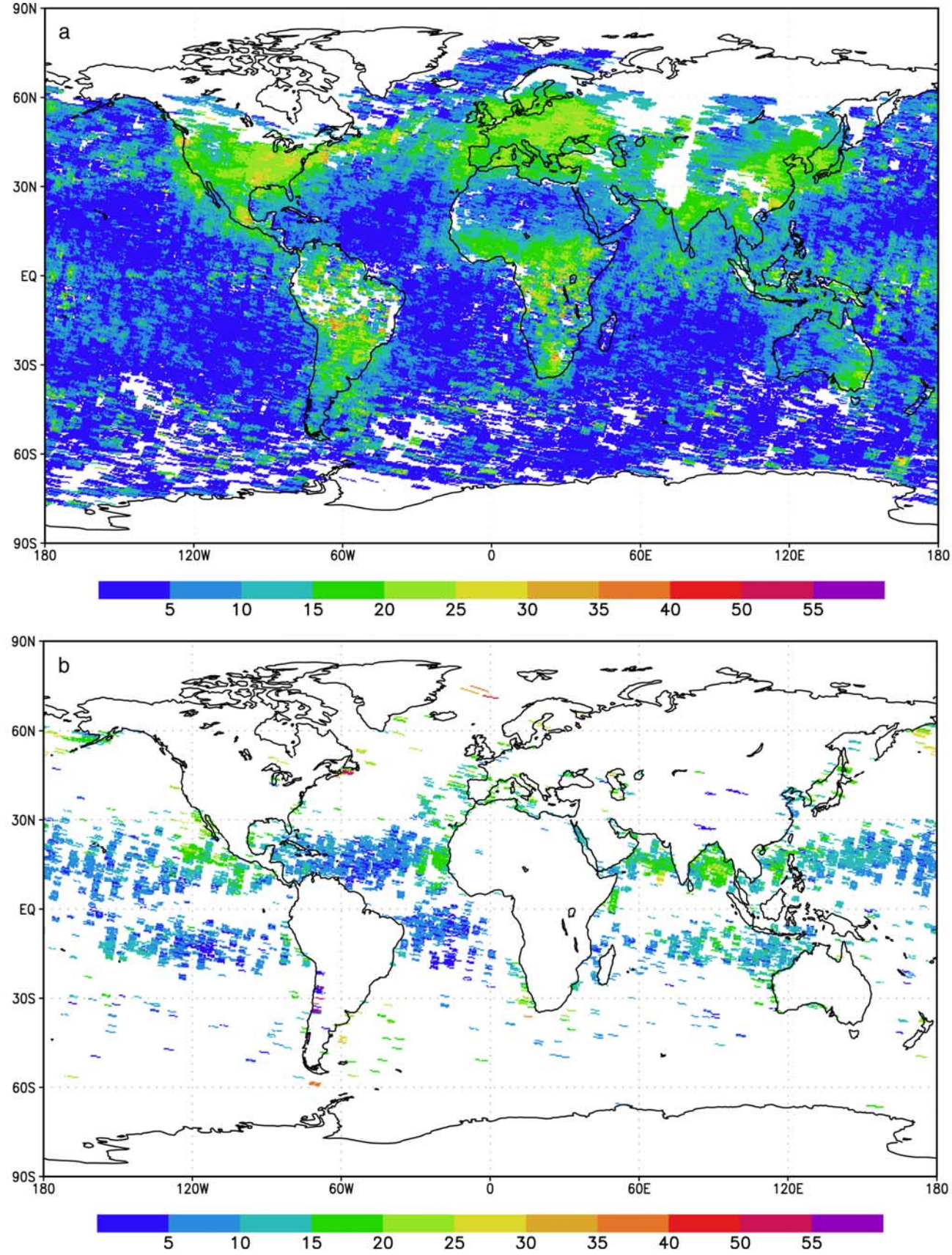

Figure 6. Uncertainty (%) in the tropospheric air mass factor for March 1997 due to uncertainties in the (a) cloud fraction, (b) cloud pressure, (c) surface albedo, and (d) profile shape. Only pixels with a cloud radiance fraction <50% were taken. In Figure 6b only pixels with a cloud pressure >800 hPa were taken.

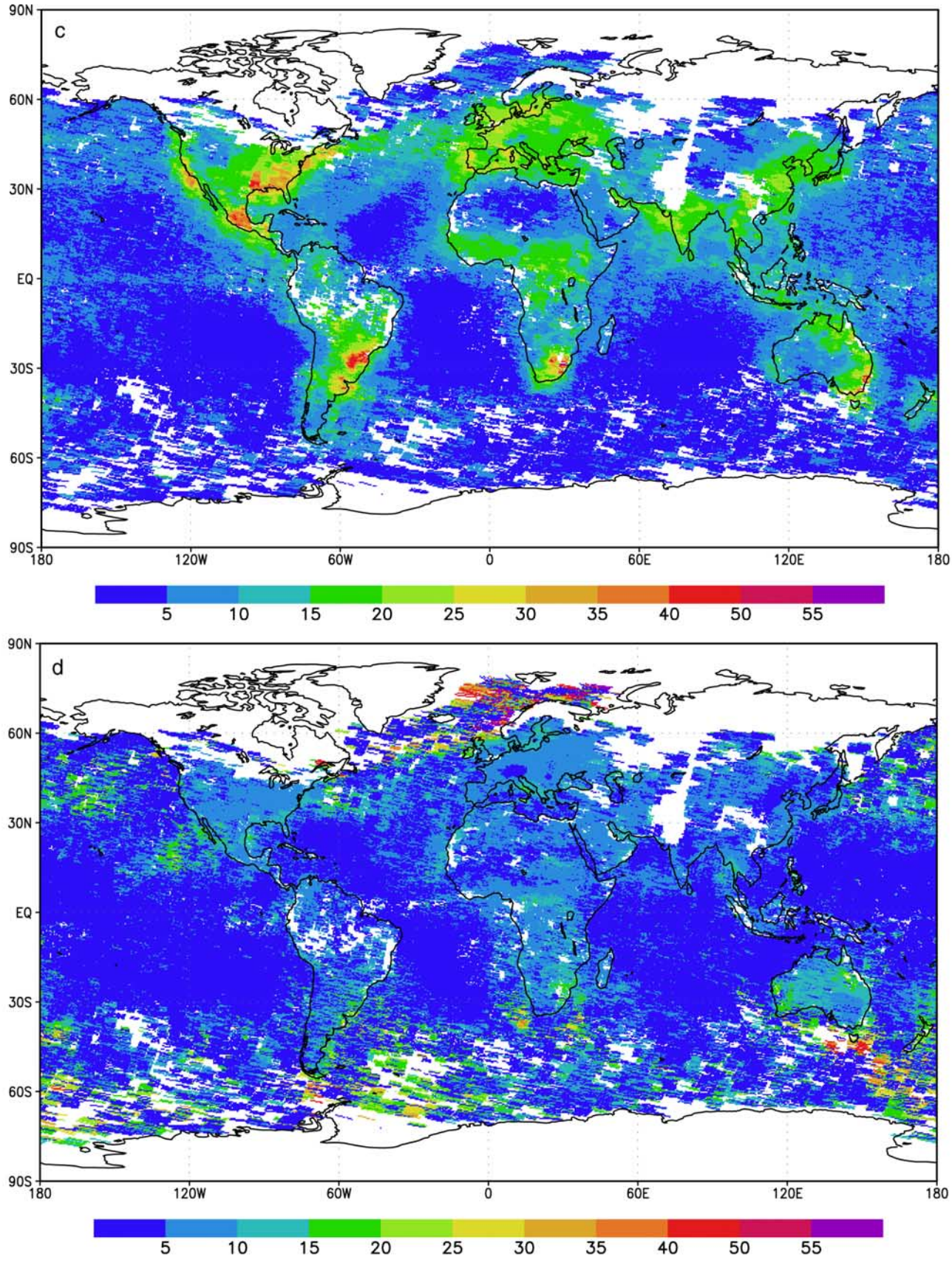

Figure 6. (continued)

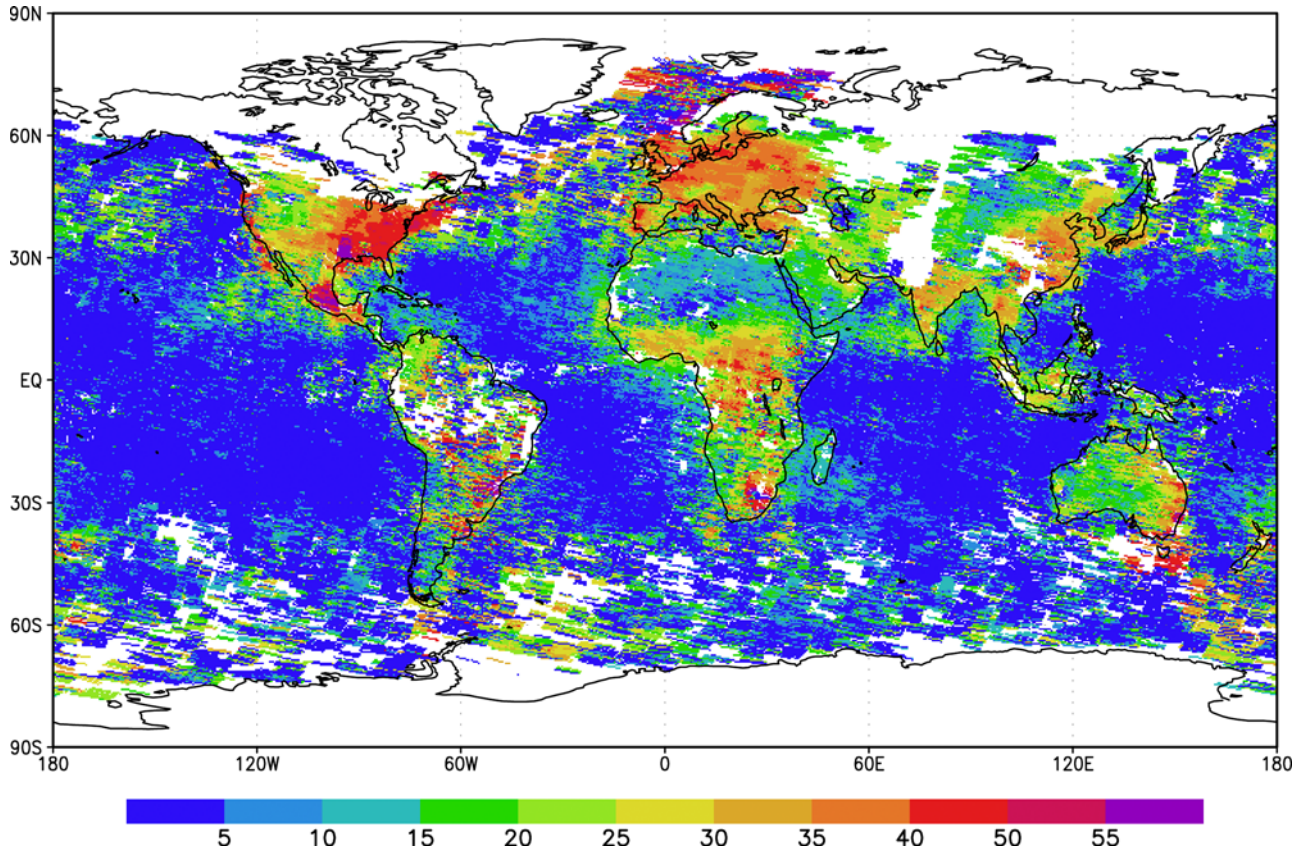

Figure 10. Uncertainty (%) in the tropospheric air mass factor for March 1997 due to uncertainties in the cloud fraction, cloud height, surface albedo and profile shape. Only pixels with a cloud radiance fraction <0.5 were taken.

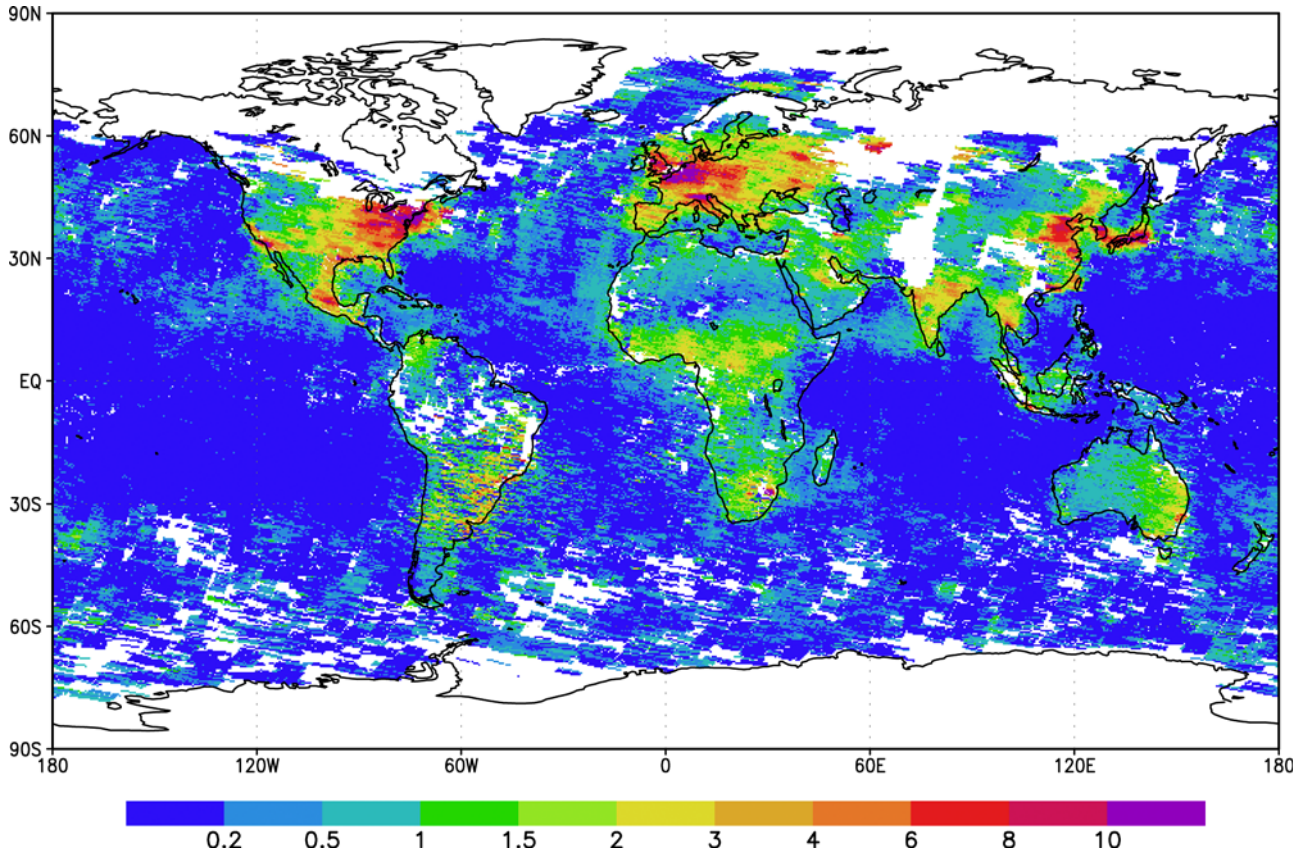

Figure 11. Monthly mean tropospheric columns for March 1997. Only pixels with a cloud radiance fraction <0.5 were taken.

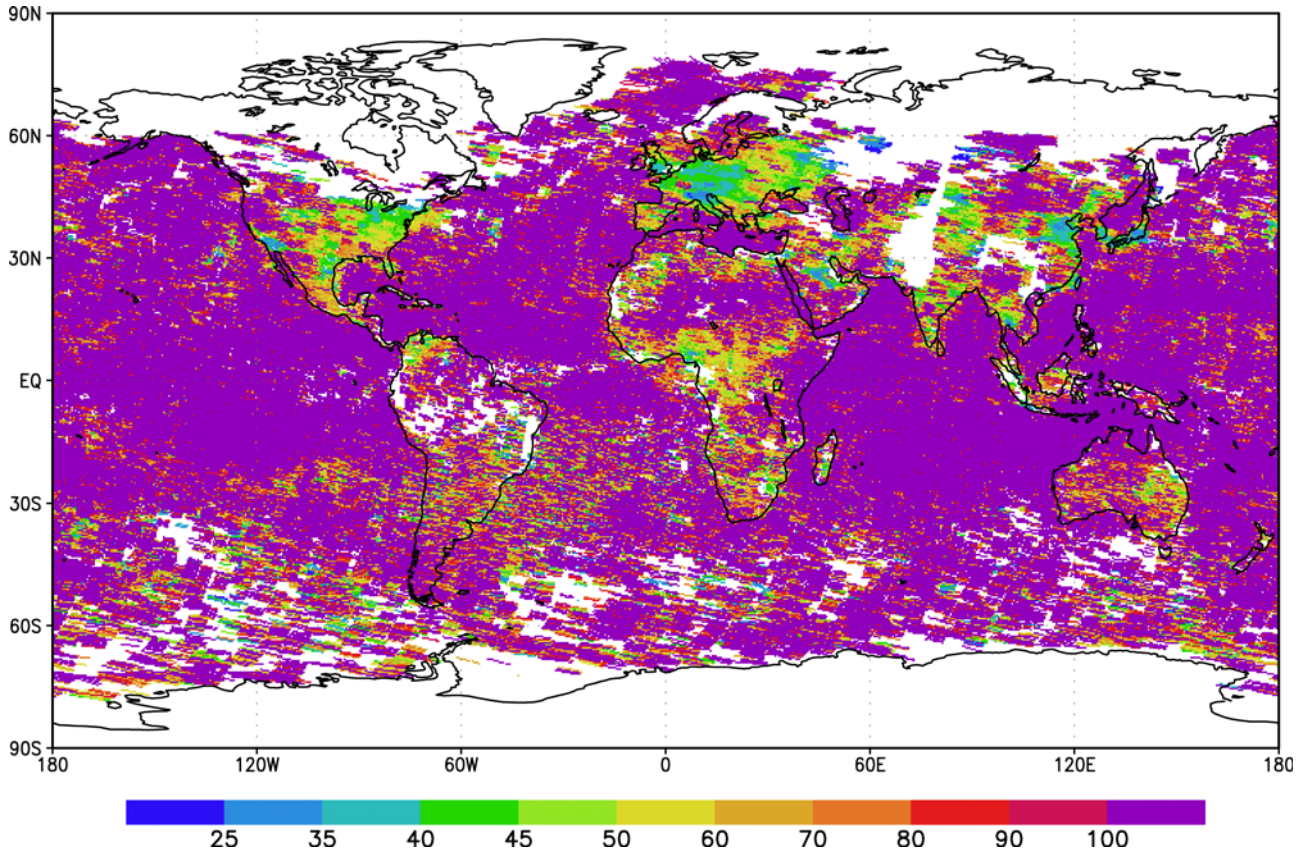

Figure 12. Relative uncertainty in tropospheric columns for March 1997. Only pixels with a cloud radiance fraction <0.5 were taken.